Check for updates

JGR Atmospheres

RESEARCH ARTICLE
10.1029/2026JD047998

Atmospheric Mechanisms of the Pattern Effect

Margaret L. Duffy[1,2], **Brian Medeiros**[1], **Andrew Gettelman**[1,3], **and Robert C. J. Wills**[4]

[1]NSF National Center for Atmospheric Research, Boulder, CO, USA, [2]University of Utah, Salt Lake City, UT, USA, [3]Pacific Northwest National Laboratory, Richland, WA, USA, [4]ETH Zürich, Zürich, Switzerland

Key Points:

- Community Atmosphere Model (CAM6) patch experiments with a satellite simulator help quantify atmospheric mechanisms of the pattern effect
- In CAM6, the pattern effect operates in part via the sensitivity of tropical marine low clouds to anomalous sea-surface temperature in regions of deep convection
- Consistently, a nonlocal stability mechanism largely mediates the pattern effect in CAM6 patch experiments and over the historical period

Supporting Information:

Supporting Information may be found in the online version of this article.

Correspondence to:

M. L. Duffy,
margaret.duffy@utah.edu

Citation:

Duffy, M. L., Medeiros, B., Gettelman, A., & Wills, R. C. J. (2026). Atmospheric mechanisms of the pattern effect. *Journal of Geophysical Research: Atmospheres*, *131*, e2026JD047998. https://doi.org/10.1029/2026JD047998

Received 14 JUL 2026
Accepted 22 SEP 2026

Author Contributions:

Conceptualization: Margaret L. Duffy
Data curation: Margaret L. Duffy
Formal analysis: Margaret L. Duffy
Investigation: Margaret L. Duffy
Methodology: Margaret L. Duffy
Software: Margaret L. Duffy
Validation: Margaret L. Duffy
Writing – original draft: Margaret L. Duffy
Writing – review & editing: Margaret L. Duffy

© 2026 The Author(s). Journal of Geophysical Research: Atmospheres published by Wiley Periodicals LLC on behalf of American Geophysical Union. This is an open access article under the terms of the Creative Commons Attribution License, which permits use, distribution and reproduction in any medium, provided the original work is properly cited.

Abstract Climate feedbacks are expected to increase over time due to the pattern effect, which describes the influence of the pattern of surface warming on global climate feedbacks. Delayed warming in the tropical east Pacific—as seen in abrupt4 × CO_2 simulations—amplifies climate feedbacks over time. There has been substantial previous work to understand the mechanisms of this pattern effect, often using ensembles of patch experiments: atmosphere-only experiments in which sea-surface temperature (SST) is systematically perturbed in patches across the globe. This previous work has highlighted lapse-rate and cloud, especially low-cloud, feedbacks in mediating the pattern effect via changes in lower tropospheric stability (LTS). Here we create an ensemble of patch experiments and use it alongside observational and reanalysis data to (a) assess the expression of the pattern effect through specific cloud feedback components, and (b) decompose the pattern effect into contributions from changes in local and nonlocal components of tropospheric stability and Walker circulation strength. These patch experiments are created using the Community Atmosphere Model, version 6 (CAM6) and are consistent with the Green's Function Model Intercomparison Project protocol. These patch experiments use a satellite simulator package, enabling an enhanced cloud-feedback decomposition, which reveals that in CAM6, tropical marine low-cloud feedbacks are primarily sensitive to (nonlocal) SST anomalies in deep-convective regions. Consistently, we find evidence that changes in the nonlocal component of LTS largely explain the relationship between the pattern of SST warming and climate feedbacks in CAM6 patch experiments and over the historical period.

Plain Language Summary The "pattern effect" describes the influence of the pattern of surface warming on global climate feedbacks. A consequence of the pattern effect is that climate feedbacks are expected to amplify over time. Specifically, delayed warming in the tropical east Pacific—as emerges several decades into abrupt4 × CO_2 simulations—causes increases in climate feedbacks. However, significant uncertainty remains regarding the extent of this increase. Here, we refine our understanding of atmospheric mechanisms of the pattern effect using the Community Atmosphere Model, version 6, forced with sea-surface temperature patches, and using interannual variability over the historical period. We find a strong role of warming in convective regions via their nonlocal influence on low clouds in subsidence regions.

1. Introduction

The equilibrium climate sensitivity (ECS) is the global-mean surface warming per doubling of CO_2 in equilibrium. The relationship between ECS and climate feedbacks is illustrated by the forcing-feedback framework

$$\Delta N = \Delta F + \Delta R \simeq \Delta F + \lambda \Delta T, \tag{1}$$

where ΔN is the net top-of-atmosphere (TOA) radiative imbalance, ΔF is the radiative forcing, and ΔR is the radiative response. The radiative response can be linearized as a function of global-mean surface temperature response and total climate feedback parameter $\lambda < 0$ according to $\Delta R \simeq \lambda \Delta T$, a good approximation. We can see the inverse relationship between ECS and λ in Equation 1 by setting $\Delta N = 0$ and the forcing to that associated with a doubling of CO_2, $\Delta F_{2\times CO_2}$, giving ECS $\equiv -\frac{\Delta F_{2\times CO_2}}{\lambda}$, with more negative λ implying a lower climate sensitivity (stabilizing) and less negative λ implying a higher climate sensitivity (amplifying). In abrupt4 × CO_2 simulations λ becomes less negative over time, implying amplified warming over time (Andrews et al., 2015; Gregory et al., 2015; Rugenstein et al., 2020; Senior & Mitchell, 2000). As a result, estimates of future climate sensitivity using the historical period will likely be underestimates (Andrews et al., 2018; Armour, 2017; Armour et al., 2024; Marvel et al., 2018). The extent to which λ increases with warming can be quantified in abrupt4 × CO_2 simulations as the difference between λ in the early and late part of the simulation:

21698996, 2026, 22, Downloaded from https://agupubs.onlinelibrary.wiley.com/doi/10.1029/2026JD047998 by Schweizerische Akademie Der Medizinischen Wissenschaften (Samw), Wiley Online Library on [21/11/2026]. See the Terms and Conditions (https://onlinelibrary.wiley.com/terms-and-conditions) on Wiley Online Library for rules of use; OA articles are governed by the applicable Creative Commons License

$\Delta\lambda = \lambda_{late} - \lambda_{early}$, where λ_{early} and λ_{late} are often diagnosed as λ averaged over years 1–20 and years 21–150, respectively. However, $\Delta\lambda$ is poorly constrained, with substantial intermodel spread (Dong et al., 2020). Since uncertainty in the time evolution of λ translates to uncertainty in the temperature response after ceased CO_2 emissions (Palazzo Corner et al., 2023), understanding and constraining the temporal evolution of λ is urgent.

The temporal evolution of λ is due primarily to evolving spatial pattern of SST warming (Andrews et al., 2015; Armour et al., 2013). That feedbacks are sensitive to the pattern of SST warming is called the "pattern effect," and it is present in model simulations and observations (Andrews et al., 2015; Ceppi & Gregory, 2017; Dong et al., 2019; Myers et al., 2023; Zhou et al., 2017). Surface warming in regions of deep convection, particularly the tropical west Pacific and Indian oceans, has a stabilizing impact on feedbacks whereas surface warming in subsidence regions, particularly the east Pacific, has an amplifying impact on feedbacks. The tropical east Pacific is an upwelling region, and therefore warming in that region is expected to be delayed compared with the west Pacific. With the differential impact of east and west Pacific warming on feedbacks found in experiments, this evolution of the SST pattern over time yields a temporal evolution in λ.

Uncertainty in the temporal evolution of λ includes uncertainty in both the pattern of SST warming $\partial \mathrm{SST}_{\mathrm{local}}/\partial T_{\mathrm{global}}$ and the atmosphere's radiative response to a given pattern of SST warming $\partial R_{\mathrm{global}}/\partial \mathrm{SST}_{\mathrm{local}}$ (Dong et al., 2020; Raghuraman & Medeiros, 2026; Wang et al., 2025). Here we focus on the latter, though we note that uncertainty in the pattern of SST warming is substantial (Coats & Karnauskas, 2017; Lee et al., 2022; Seager et al., 2022; Watanabe et al., 2024; Wills et al., 2022). Here we refer to mechanisms of the atmosphere's response to a given pattern of SST warming as "atmospheric mechanisms" of the pattern effect to distinguish from mechanisms setting the pattern of SST warming.

Atmospheric mechanisms of the pattern effect can be quantitatively estimated in atmosphere-only general circulation models (AGCMs) using ensembles of patch experiments in which SST anomalies are imposed at a different location in each ensemble member. The impact of these SST anomalies on the atmosphere can then be reconstructed using a Green's function approach (Bloch-Johnson et al., 2024; Dong et al., 2019; A. I. L. Williams et al., 2023; Zhou et al., 2017). This Green's function approach has been implemented in a number of AGCMs. In all AGCMs, warming over the tropical west Pacific has a strong stabilizing influence on feedbacks and warming over the tropical east Pacific has a somewhat amplifying influence on feedbacks (Bloch-Johnson et al., 2024).

Due to its importance and robust presence in global climate models (GCMs), understanding of the atmospheric mechanisms of the pattern effect is continuously being refined. Most previous work indicates that the pattern effect operates primarily through cloud and lapse-rate feedbacks in GCMs (Andrews & Webb, 2018; Dong et al., 2019). In particular, Dong et al. (2019) find a very stabilizing shortwave (SW) cloud feedback when the convective regions of the west Pacific are warmed, with partial compensation from the longwave (LW) cloud feedback. This SW cloud feedback is thought to be the result of changes in low clouds nonlocally due to changes in lower tropospheric stability (LTS) (Andrews & Webb, 2018; A. I. L. Williams et al., 2023). Changes in tropospheric stability can also correspond to a lapse-rate feedback (Andrews & Webb, 2018). Dong et al. (2019) and Andrews and Webb (2018) both find a very strong lapse-rate feedback, but it is largely compensated by the water-vapor (WV) feedback. Both use fixed specific-humidity kernels, which yields larger compensation than when fixed relative humidity (RH) kernels are used (Held & Shell, 2012).

The relationship between warming and these feedbacks involves multiple processes, which have sometimes been separately discussed as mechanisms of the pattern effect. In particular, the roles of tropospheric stability and Walker circulation (WC) strength have been previously discussed. Our goal is to evaluate their role in the pattern effect and their relationship to one another.

1.1. Tropospheric Stability

Previous work indicates that changes in low clouds in tropical subsidence regions underlie the pattern effect. These changes in low clouds are correlated with changes in lower-tropospheric inversion strength as measured by estimated inversion strength (EIS; Ceppi & Gregory, 2017), lower tropospheric stability (LTS; Andrews & Webb, 2018), estimated cloud-top entrainment index (ECTEI; Kawai et al., 2017), or convective instability index (CII; A. I. L. Williams et al., 2023). Lower-tropospheric inversion strength can be modified through either a "local stability inversion" or "nonlocal stability inversion" mechanism.

21698996, 2026, 22, Downloaded from https://agupubs.onlinelibrary.wiley.com/doi/10.1029/2026JD047998 by Schweizerische Akademie Der Medizinischen Wissenschaften (Samw), Wiley Online Library on [21/11/2026]. See the Terms and Conditions (https://onlinelibrary.wiley.com/terms-and-conditions) on Wiley Online Library for rules of use; OA articles are governed by the applicable Creative Commons License

- *Local stability inversion*: Local surface warming tends to decrease inversion strength near the surface and, as a result, decrease low-cloud amount (Alessi & Rugenstein, 2023; A. I. L. Williams et al., 2023).
- *Nonlocal stability inversion*: Tropospheric stability can also be controlled by warming or cooling of the free troposphere, which can be controlled nonlocally. Warming in deep convective regions is communicated to the free troposphere, which is communicated laterally by free-tropospheric waves (maintaining weak temperature gradients). This tends to increase the inversion strength and, as a result, increase the low-cloud amount (Alessi & Rugenstein, 2023; Andrews & Webb, 2018; Rugenstein et al., 2023; A. I. L. Williams et al., 2023). This nonlocal stability inversion mechanism is consistent with a "circus tent" model introduced by A. I. L. Williams et al. (2023) to explain the asymmetry in responses to cool and warm patches in patch experiments.

1.2. Walker Circulation Strength

While tropospheric stability has prevailed as the leading mechanistic explanation, some previous work has hypothesized that the pattern effect operates in part through the influence of SST on the large-scale circulation (Mackie et al., 2025; Stevens et al., 2016). In particular, the strength of the Pacific Walker circulation (WC) varies with the zonal SST gradient over the tropical Pacific; this zonal SST gradient is key to the pattern effect (Andrews et al., 2015; Dong et al., 2019; Lee et al., 2022; Watanabe et al., 2024; Wills et al., 2022). The WC is a zonal circulation with ascent and high clouds over the warmer west Pacific and descent and low clouds over the cooler east Pacific (Duffy & O'Gorman, 2023; Lee et al., 2022). WC strength, and thus the corresponding clouds, are highly sensitive to the zonal SST gradient across the tropical Pacific (Lee et al., 2022). Further, changes in WC strength are associated with changes in radiation, especially cloud-radiative effects (Duffy & O'Gorman, 2023). Therefore, we expect some relationship between WC strength, TOA radiation, and the pattern effect. However, the role of WC strength and the associated feedbacks in the pattern effect has not been thoroughly documented. Similar to tropospheric stability, there are numerous metrics for WC strength (Kosovelj & Zaplotnik, 2023).

This paper aims to improve our understanding of the atmospheric mechanisms of the pattern effect using (a) an ensemble of patch experiments and (b) interannual variability over the historical period. We create an ensemble of patch experiments with the Community Atmosphere Model, version 6 (CAM6; Danabasoglu et al., 2020). Unlike many previous patch experiment ensembles, the CAM6 ensemble is created with the CFMIP observation simulator package (COSP) enabled (Bodas-Salcedo et al., 2011), allowing for a decomposition of cloud feedbacks into the six assessed feedback components of Sherwood et al. (2020). Using this new ensemble of CAM6 patch experiments along with observations of the historical period, we address the following questions:

1. What are the contributions to $\partial R_{\text{global}}/\partial \text{SST}_{\text{local}}$ from each feedback component in CAM6?
2. Which, if any, metrics of tropospheric stability and WC strength can explain $\partial R_{\text{global}}/\partial \text{SST}_{\text{local}}$ in CAM6 patch experiments and historical interannual variability?
3. Finally, we find that WC strength does not robustly mediate the pattern effect. Why not?

This work is timely because a Green's Function Model Intercomparison Project (GFMIP) protocol was recently published and GFMIP will yield additional ensembles of patch experiments (Bloch-Johnson et al., 2024).

2. Methods

2.1. CAM6 Patch Ensemble

Ensembles of patch experiments have been created using a variety of AGCMs to evaluate the sensitivity of the atmosphere to local SST anomalies (Bloch-Johnson et al., 2024; Dong et al., 2019; A. I. L. Williams et al., 2023; Zhou et al., 2017). Here we create an ensemble of CAM6 patch experiments which are part of the Green's Function Model Intercomparison Project (GFMIP; Bloch-Johnson et al., 2024; Duffy, 2026b). We run a control experiment for 12 years and each patch experiment for 8 years, long enough for stable simulations and to capture the dominant signal in $\partial R_{\text{global}}/\partial \text{SST}_{\text{local}}$ (Figure S1 in Supporting Information S1). The SST perturbation for each patch experiment is elliptic with a peak amplitude of 2 K and is as in Equation 1 of Bloch-Johnson et al. (2024). The CAM6 patch ensemble setup is mostly consistent with the GFMIP protocol, except it only considers patches which are at least 25% ocean covered (see Figure S2 in Supporting Information S1 for the 92 patches), it is run for 8 years instead of 10, and it uses F2000climo SSTs whereas the GFMIP protocol uses the climatology of AMIP SSTs. Both use specified, annually-repeating SST and sea-ice area, but differ in their averaging periods (1995–2005 in the CAM6 ensemble vs. 1971–2020 for GFMIP). The use of F2000climo SSTs

21698996, 2026, 22, Downloaded from https://agupubs.onlinelibrary.wiley.com/doi/10.1029/2026JD047998 by Schweizerische Akademie Der Medizinischen Wissenschaften (Samw), Wiley Online Library on [21/11/2026]. See the Terms and Conditions (https://onlinelibrary.wiley.com/terms-and-conditions) on Wiley Online Library for rules of use; OA articles are governed by the applicable Creative Commons License

makes the CAM6 patch experiments directly comparable with the CAM6 perturbed parameter ensemble (PPE; Eidhammer et al., 2024). That is, they are run using CAM6.3.026 and using F2000climo. Note that this is a developmental version of CAM6 and differs slightly from the scientific releases. While we do not compare the CAM6 patch experiments with the CAM6 PPE here, CAM6 users may benefit from these two compatible sets of experiments. Cooling patch experiments with amplitude −2 K are also run for 4 years each and are available through GFMIP, but we do not make use of these cooling experiments here. The CAM6 patch experiments are run with the COSP enabled (Bodas-Salcedo et al., 2011), allowing for more detailed cloud feedback decomposition than previous patch experiment ensembles, which we use in Section 3. The first year of each patch experiment is removed from our analyses to account for spinup. Finally, in addition to the control experiment with F2000climo, we also run a CAM6 historical experiment which is forced with transient SSTs and boundary conditions from the years 1979–2014. We will use this CAM6 historical experiment in Sections 4.2, 5.2, and 6.

Considering Equation 1, the patch experiments, like other AGCM experiments, differ from fully-coupled GCM experiments. They quickly reach a steady-state but never reach an equilibrium (i.e., $\Delta N \neq 0$). Further, as the patch experiments are forced with an SST perturbation rather than a change in CO_2, $\Delta F = 0$ and we have $\Delta N = \Delta R$. Despite these differences, estimates of λ are consistent between coupled and atmosphere-only simulations (Qin et al., 2022; Ringer et al., 2014), so these experiments are appropriate for studying the pattern effect.

Patch experiments are useful for evaluating the sensitivity of a given feature of the atmosphere, such as global-mean radiative response, to the pattern of SST using an atmospheric Green's function approach (Barsugli & Sardeshmukh, 2002; Bloch-Johnson et al., 2024; Zhou et al., 2017). However, we note that applying an atmospheric Green's function reconstruction to the CAM6 patch experiments does not recreate the global-mean radiative feedback of for example a uniform warming experiment. This is not entirely surprising because there is no a priori reason to expect linear additivity. Other patch ensembles suffer the same nonadditivity (Quan et al., 2024). We demonstrate the patch nonadditivity using the CAM6 historical and uniform 2 K warming experiments (Figure S3 in Supporting Information S1). In both the historical and uniform 2 K warming experiments, the Green's function reconstruction tends to overestimate the magnitude of ΔR (Figure S3 in Supporting Information S1). Because of the nonadditivity, the CAM6 patch experiments cannot be interpreted as a decomposition of a uniform warming experiment. Despite the nonadditivity, the patch experiments are an appropriate tool for evaluating the processes underlying the response of radiative feedbacks to temperature perturbations in CAM6.

In the CAM6 patch ensemble, ΔR is calculated using radiative kernels (Soden et al., 2008). Cloud feedbacks are calculated using the cloud radiative kernels of Zelinka et al. (2012a, 2012b), which make use of cloud-top pressure and cloud optical depth histograms. Therefore, cloud feedbacks can be partitioned into the six assessed components of Sherwood et al. (2020) as in Zelinka et al. (2022). Noncloud feedbacks are calculated using CAM5 radiative kernels (Pendergrass et al., 2018) and implemented using `ClimKern` (Janoski et al., 2025). We use their "method 3" option to calculate humidity feedbacks in `ClimKern` because in practice this yields a smaller residual than the other methods with our data set. Otherwise, we use the `ClimKern` default parameters. The CAM5 radiative kernels are derived from the same radiation scheme as used in CAM6. Nonetheless, we note that our results may be sensitive to the choice of kernel (Janoski et al., 2025).

2.2. Observations and Reanalysis Data Over the Historical Period

We evaluate the metrics of the pattern effect over the historical period in three data sets. We use the CAM6 historical experiment described above, which is a CAM6 historical experiment forced with SSTs and boundary conditions from the years 1979–2014 (Danabasoglu et al., 2020). We use monthly-mean ERA5 data from 1979 to 2022 (Hersbach et al., 2023), data from Clouds and Earth's Radiant Energy System (CERES) Energy Balanced and Filled (EBAF) Edition 4.2 from 2001 to 2022 (NASA/LARC/SD/ASDC, 2022), and SST from NOAA NCEP Optimum Interpolation (OI) SST (B. Huang et al., 2021).

Unlike the CAM6 patch experiments, which are forced with anomalous SST, the real atmosphere and CAM6 historical experiment have varying atmospheric constituents that induce a radiative forcing. Therefore, the TOA radiative imbalance ΔN represents a combination of forcing and radiative response (Equation 1). We approximate the component of TOA radiative imbalance ΔN from the radiative response ΔR using radiative kernels as described in Kramer et al. (2021). Radiative feedbacks from different data sources are evaluated with the associated kernels where possible. That is, ERA5 kernels (H. Huang & Huang, 2023) are used to calculate

radiative feedbacks using ERA5 data, CERES kernels (Thorsen et al., 2018) are used to calculate radiative feedbacks using CERES data, and CAM5 kernels (Pendergrass et al., 2018) are used to calculate feedbacks using CAM6 historical experiment data. These calculations are applied using `ClimKern` (Janoski et al., 2025).

2.3. Metrics of the Pattern Effect

In Section 4 we will evaluate the metrics of the proposed atmospheric pattern effect mechanisms described in the introduction, separately quantifying the role of local stability inversion, nonlocal stability inversion, and WC strength. There are numerous metrics which could reasonably be selected to represent each of these three mechanisms. Here we select a default metric to measure each mechanism, and we compare with alternative metrics. Note that although we discuss the role of these three mechanisms separately, we do not assume a priori they are independent from one another.

There are numerous metrics of tropospheric stability. The simplest is the lower tropospheric stability (LTS), the difference in potential temperature θ between 700 hPa and near the surface (Klein & Hartmann, 1993). In practice, we use 2-m temperature for the near-surface θ. Wood and Bretherton (2006) propose a refinement of LTS called the EIS, which they argue is a more climate-invariant measure of inversion strength than LTS. Here we use the following expression for EIS

$$\mathrm{EIS} = \mathrm{LTS} - \Gamma_{700} Z_{700} + \Gamma_{LCL} Z_{LCL}, \tag{2}$$

where Γ is the moist adiabatic potential temperature gradient, Z_{700} is the height at 700 hPa, and Z_{LCL} is the height of the lifted condensation level (LCL). Note that Γ_{700} and Γ_{LCL} are often replaced with Γ_{850} (see Wood and Bretherton (2006) for details), but we do not do that here for clean separation between local and nonlocal contributions to EIS. We estimate the LCL as in Espy (1836) using the temperature and dewpoint temperature at 1,000 hPa, and then we calculate Γ using temperature and pressure from the model level nearest the LCL. Kawai et al. (2017) introduce another measure of inversion strength, the ECTEI, which they assert is even more highly correlated with low cloud cover than EIS. ECTEI is defined as

$$\mathrm{ECTEI} = \mathrm{EIS} - \beta \frac{L}{c_p}(q_0 - q_{700}), \tag{3}$$

where $\beta = 0.23$ (see Kawai et al. (2017) for details), L is the latent heat of vapourization, c_p is the specific heat of air at constant pressure, q_0 is specific humidity at 1,000 hPa, and q_{700} is the specific humidity at 700 hPa. Further, in the circus tent model of A. I. L. Williams et al. (2023) inversion strength is measured using a CII of I. N. Williams and Pierrehumbert (2017), which is defined as

$$\mathrm{CII} = h_0 - h^*_{500}, \tag{4}$$

where h^*_{500} is the saturation moist static energy (MSE) at 500 hPa and h_0 is the MSE at 1,000 hPa. Each of these metrics can be separated into local (near surface) and nonlocal (free tropospheric) contributions. Using the sign convention of CII (local minus nonlocal) for all four metrics, the local contribution to LTS is θ_s and the nonlocal contribution is $-\theta_{700}$. The local contribution to EIS is $\theta_s - \Gamma_{LCL} Z_{LCL}$ and the nonlocal contribution is $-\theta_{700} + \Gamma_{700} Z_{700}$. The local contribution to ECTEI is $\theta_s - \Gamma_{LCL} Z_{LCL} + \beta \frac{L}{c_p} q_0$ and the nonlocal contribution is $-\theta_{700} + \Gamma_{700} Z_{700} - \beta \frac{L}{c_p} q_{700}$. The local contribution to CII is h_0 and the nonlocal contribution is $-h^*_{500}$.

By default, we measure local stability inversion using the local portion of the CII (i.e., h_0) averaged over oceanic subsidence regions between 60°S and 60°N to encompass the full range of regions evaluated in Klein and Hartmann (1993) and Wood and Bretherton (2006). Subsidence regions are defined as regions where time- and annual-mean ω_{500} is positive over the relevant control period, consistent with Bony and Dufresne (2005). By default, we measure nonlocal stability inversion using the nonlocal portion of the CII (i.e., $-h^*_{500}$) averaged over oceanic regions from 60°S and 60°N. In Section 5 we will evaluate the sensitivity to choice of metric and region of averaging.

21698996, 2026, 22, Downloaded from https://agupubs.onlinelibrary.wiley.com/doi/10.1029/2026JD047998 by Schweizerische Akademie Der Medizinischen Wissenschaften (Samw), Wiley Online Library on [21/11/2026]. See the Terms and Conditions (https://onlinelibrary.wiley.com/terms-and-conditions) on Wiley Online Library for rules of use; OA articles are governed by the applicable Creative Commons License

21698996, 2026, 22, Downloaded from https://agupubs.onlinelibrary.wiley.com/doi/10.1029/2026JD047998 by Schweizerische Akademie Der Medizinischen Wissenschaften (Samw), Wiley Online Library on [21/11/2026]. See the Terms and Conditions (https://onlinelibrary.wiley.com/terms-and-conditions) on Wiley Online Library for rules of use; OA articles are governed by the applicable Creative Commons License

There are numerous measures of WC strength (Kosovelj & Zaplotnik, 2023). By default, we measure WC strength using a streamfunction index of WC strength ψ_{500} because, of the various metrics evaluated by Kosovelj and Zaplotnik (2023), the stream function index of WC strength ψ_{500} is the least correlated with zonal SST gradient, another measure of WC strength. The low correlation is beneficial for our purposes because the zonal SST gradient is imposed in the patch simulations. The stream function index of WC strength ψ_{500} is calculated as the maximal streamfunction at 500 hPa between 90°E and 80°W calculated using the zonal component of the total wind. See Kosovelj and Zaplotnik (2023) for details. In addition to the default measure, we compare with one alternative measure of WC strength: $\overline{\omega}_{e-w}$, which is the negative of the difference between vertically-integrated vertical velocity over the west Pacific and east Pacific boxes. This is the negative of $\overline{\omega}_{w-e}$ used in Duffy and O'Gorman (2023) so that a stronger WC is more positive. In calculating $\overline{\omega}_{e-w}$ both boxes run from 5°S to 5°N (Vecchi et al., 2006). The west Pacific box covers 80°E to 160°E and the east Pacific box covers 160°W to 80°W.

3. Detailed Feedback Decomposition in CAM6 Patch Ensemble

Here we use the Green's function approach to evaluate the influence of SST perturbations on the total radiative response ΔR and its components in the CAM6 patch ensemble described in Section 2.1. In these experiments, the total radiative response and its components are proportional to the feedback parameter λ as $\lambda \simeq \Delta R/\Delta T$. This approach yields maps of the *global-mean* radiative response as a function of *local* SST perturbation ($\partial R_{\text{global}}/\partial \text{SST}_{\text{local}}$, though we use $\partial R/\partial \text{SST}$ as shorthand from here forward), as shown in Figure 1a. However, it is worth noting that the spatial pattern of the response to each patch can be complex (Figure S4 in Supporting Information S1), and this complexity is lost by only showing the global-mean response to each patch. Consistent with patch experiments using other models, we find a strong stabilizing effect of warming over the tropical west Pacific, with an amplifying effect of warming over the tropical east Pacific (Figure 1a; Bloch-Johnson et al., 2024; Dong et al., 2019; A. I. L. Williams et al., 2023; Zhou et al., 2017).

We decompose the total radiative response into its contributions from the Planck, lapse-rate, RH, albedo, and cloud feedbacks (Figure 1). These five contributions approximately sum to the total (Figure S5 in Supporting Information S1). Previous authors have found a strong role of cloud and lapse-rate feedbacks (Andrews & Webb, 2018; Dong et al., 2019). However, the lapse-rate feedback is largely compensated by the water-vapor (WV) feedback when the decomposition is done with specific humidity as the state variable (Held & Shell, 2012; Randall et al., 2007). Here we use a fixed RH kernel in Figure 1 and compare with a fixed specific-humidity kernel in Figure S6 in Supporting Information S1. Consistent with the results from CAM4 patch experiments, the lapse-rate and cloud feedbacks have the strongest contribution to the pattern effect, with a partially opposing effect of the WV feedback when specific humidity is used as the state variable (Figure S6 in Supporting Information S1; Dong et al., 2019). However, the lapse-rate feedback is small when fixed RH kernels are used (Figure 1; Held & Shell, 2012). The cloud feedback is the same with either state variable, and is a dominant term in the decomposition.

Since cloud feedbacks are the dominant contribution to $\partial R/\partial \text{SST}$ (Figure 1), we further decompose the cloud feedback into contributions from six cloud feedback components: high-cloud altitude, tropical marine low-cloud, tropical anvil cloud area, land cloud amount, midlatitude marine low-cloud amount, and high-latitude low-cloud optical depth feedbacks (Figure 2), as in Sherwood et al. (2020). This decomposition was not conducted with earlier patch experiment ensembles because it requires the COSP simulator feature to be enabled when the patch experiments are run (Bodas-Salcedo et al., 2011; Zelinka et al., 2012a, 2012b).

The cloud feedback decomposition reveals that the tropical marine low-cloud feedback dominates the pattern effect's influence on the total cloud feedback, especially where cloud feedback sensitivity is negative (Figure 2c). It is notable that the impact of the pattern effect on the tropical marine low-cloud feedback is not local, with warming in deep convective regions rather than local warming influencing the tropical marine low-cloud feedback. For reference, the hatching in Figure 3 denotes subsidence regions. We will further discuss this in Section 4.1.2. The decomposition also reveals some negative feedbacks from the high-cloud altitude (Figure 2b) and tropical anvil cloud area feedbacks (Figure 2d) with SST warming. The land cloud, midlatitude marine low-cloud amount, and high-latitude low-cloud optical depth feedback contributions are small (Figures 2e, 2f, and 2g). The unassessed component of the feedbacks is substantial, contributing a stabilizing feedback with SST warming in most regions (Figure 2h), and is further decomposed in Figure S7 in Supporting Information S1. Surprisingly, the positive regions of $\partial R/\partial \text{SST}$ result from a combination of RH, high-cloud altitude, and anvil cloud area

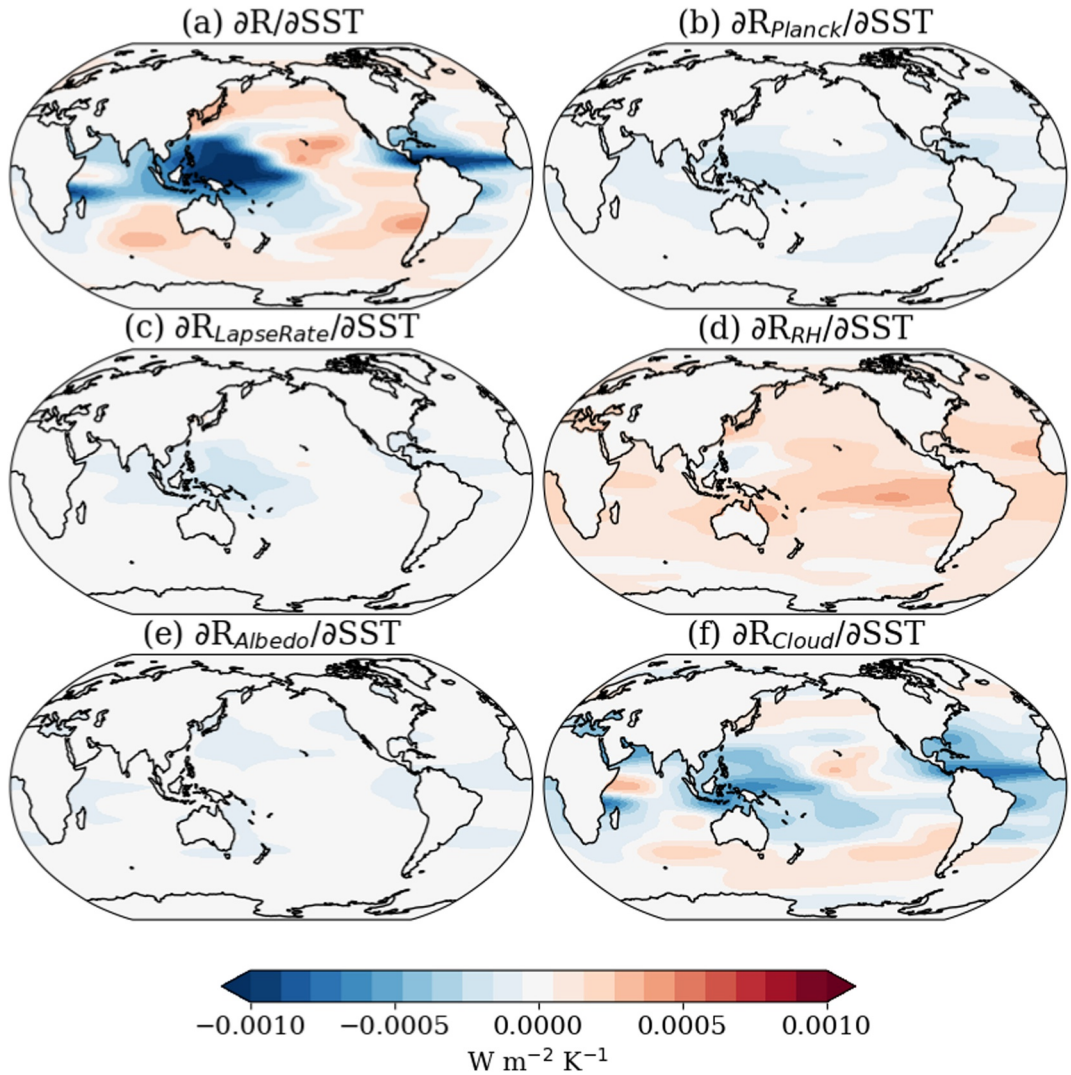


Figure 1. Response of global-mean top-of-atmosphere (TOA) radiation per degree of grid-box sea-surface temperature warming (W m^{-2} K^{-1}) for (a) the total change in TOA radiation and separated into contributions from (b) the Planck feedback, (c) the lapse-rate feedback, (d) the relative humidity feedback, (e) the albedo feedback, and (f) the total cloud feedback. In all maps, blue represents a negative (stabilizing) feedback and red represents a positive (amplifying) feedback. Note that the magnitude is resolution dependent and therefore may not easily compare with results from other models.

feedbacks, not from the low-cloud feedbacks. The strong role of the RH feedback for east-Pacific warming is consistent with work identifying a strong WV feedback for El Niño variability (Hu et al., 2016). The positive high-cloud altitude feedback is consistent with the observed response to climate warming. The anvil cloud area feedback is a balance between larger-magnitude SW and LW feedbacks and as a result the net magnitude of this feedback is difficult for models to estimate (Raghuraman et al., 2024). We encourage future ensembles of patch experiments to enable the COSP satellite simulator so that the robustness of the decomposition in Figure 2 and Figure S7 in Supporting Information S1 can be evaluated.

Overall, in CAM6, we find that cloud feedbacks dominate the pattern effect. The negative sensitivity in deep convective regions is due largely to the sensitivity of tropical marine low clouds to SST warming. Notably, *changes in tropical marine low clouds are largely due to nonlocal warming in regions of deep convection* (Figure 2c). This is consistent with a strong role of the nonlocal stability inversion mechanism. We will evaluate mechanisms in the next section.

21698996, 2026, 22, Downloaded from https://agupubs.onlinelibrary.wiley.com/doi/10.1029/2026JD047998 by Schweizerische Akademie Der Medizinischen Wissenschaften (Samw), Wiley Online Library on [21/11/2026]. See the Terms and Conditions (https://onlinelibrary.wiley.com/terms-and-conditions) on Wiley Online Library for rules of use; OA articles are governed by the applicable Creative Commons License

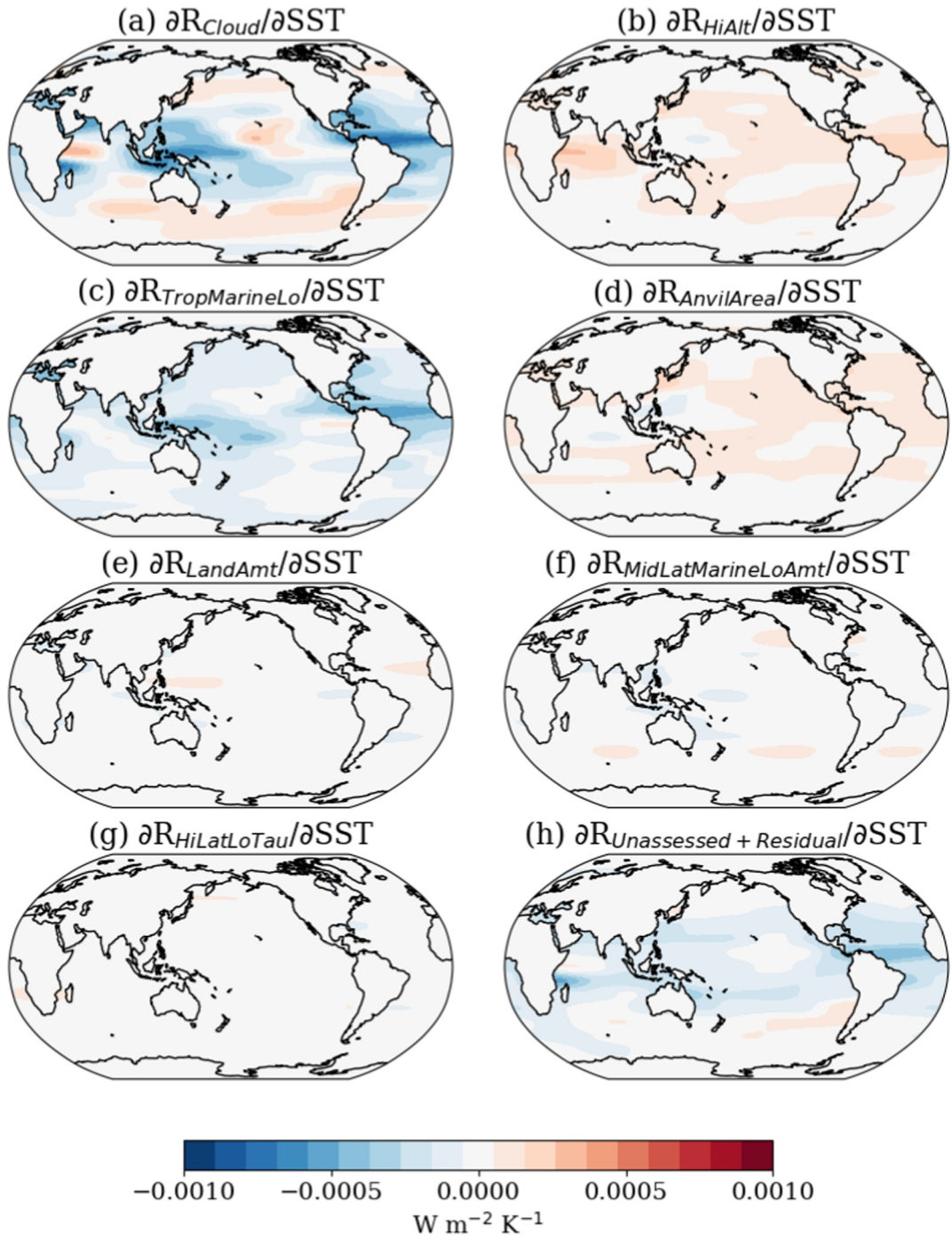


Figure 2. The contributions to the response of global-mean top-of-atmosphere radiation per degree of grid-box sea-surface temperature warming (W m^{-2} K^{-1}) from (a) the cloud feedback and separated into contributions from (b) the high-cloud altitude feedback, (c) the tropical marine low-cloud feedback, (d) the tropical anvil cloud area feedback, (e) the land cloud amount feedback, (f) the midlatitude marine low-cloud amount feedback, (g) the high-latitude low-cloud optical depth feedback, and (h) the unassessed cloud feedback. In all maps, blue represents a negative (stabilizing) feedback and red represents a positive (amplifying) feedback. Note that the magnitude is resolution dependent and therefore may not easily compare with results from other models.

21698996, 2026, 22, Downloaded from https://agupubs.onlinelibrary.wiley.com/doi/10.1029/2026JD047998 by Schweizerische Akademie Der Medizinischen Wissenschaften (Samw), Wiley Online Library on [21/11/2026]. See the Terms and Conditions (https://onlinelibrary.wiley.com/terms-and-conditions) on Wiley Online Library for rules of use; OA articles are governed by the applicable Creative Commons License

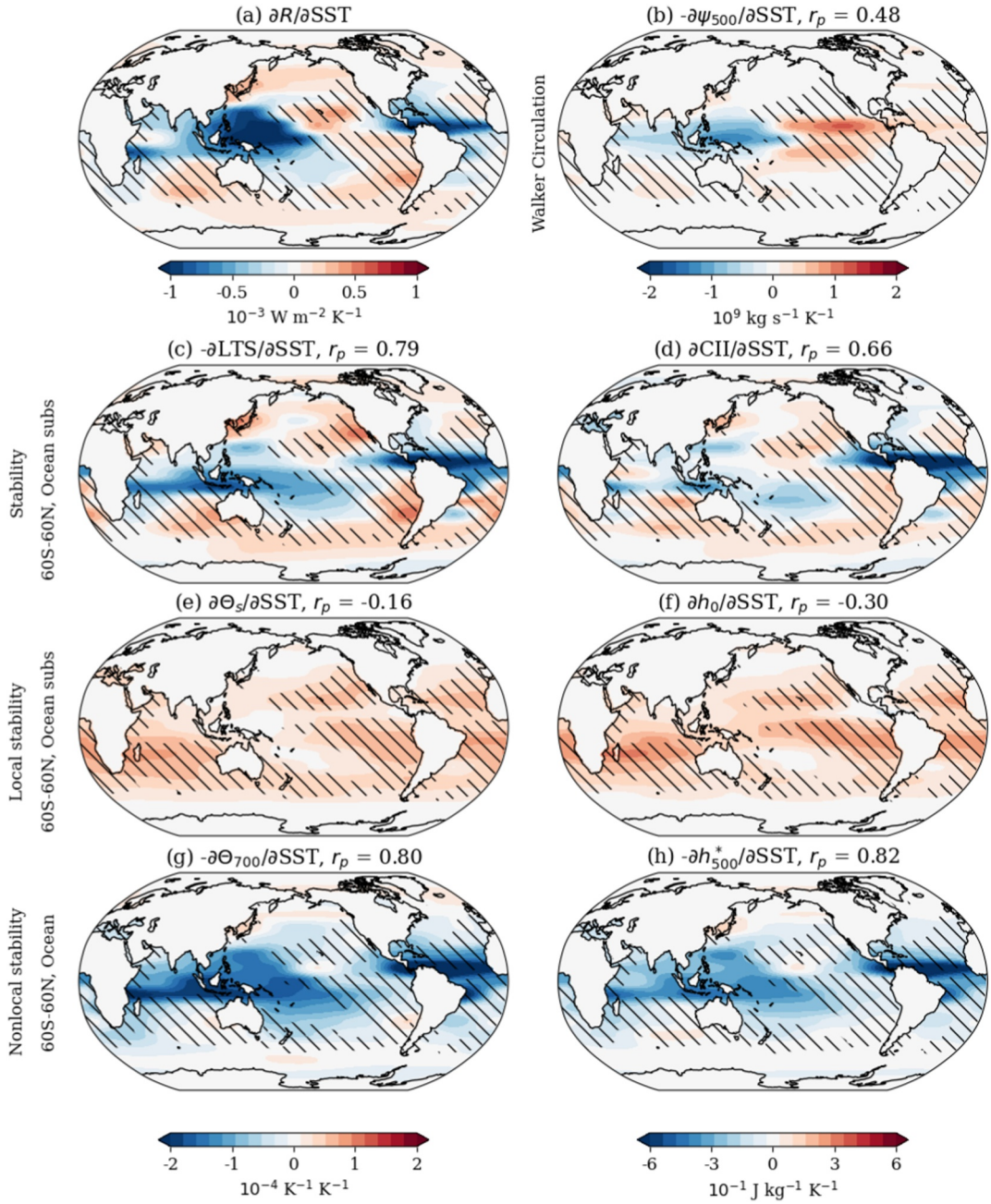


Figure 3. Response per degree of grid-box sea-surface temperature (SST) warming for (a) the total change in top-of-atmosphere radiation (W m^{-2} K^{-1}), (b) Walker circulation strength as measured using $-\psi_{500}$ per degree of grid-box SST warming (kg s^{-1} K^{-1}), (c) the tropospheric stability mechanism as measuring using lower tropospheric stability (K K^{-1}), (d) the tropospheric stability mechanism as measuring using convective instability index (J kg^{-1} K^{-1}), (e) the local stability inversion component of the tropospheric stability mechanism as measured using θ_s, (f) the local stability inversion component of the tropospheric stability mechanism as measured using h_0, (g) the nonlocal stability inversion component of the tropospheric stability mechanism as measured using $-\theta_{700}$, and (h) the nonlocal stability inversion component of the tropospheric stability mechanism as measured using $-h^*_{500}$. Hatches denote regions of climatological subsistence ($\omega_{500} > 0$) over oceans between 60°S and 60°N. Note that the magnitudes are resolution dependent and therefore may not easily compare with results from other models.

21698996, 2026, 22, Downloaded from https://agupubs.onlinelibrary.wiley.com/doi/10.1029/2026JD047998 by Schweizerische Akademie Der Medizinischen Wissenschaften (Samw), Wiley Online Library on [21/11/2026]. See the Terms and Conditions (https://onlinelibrary.wiley.com/terms-and-conditions) on Wiley Online Library for rules of use; OA articles are governed by the applicable Creative Commons License

21698996, 2026, 22, Downloaded from https://agupubs.onlinelibrary.wiley.com/doi/10.1029/2026JD047998 by Schweizerische Akademie Der Medizinischen Wissenschaften (Samw), Wiley Online Library on [21/11/2026]. See the Terms and Conditions (https://onlinelibrary.wiley.com/terms-and-conditions) on Wiley Online Library for rules of use; OA articles are governed by the applicable Creative Commons License

4. Evaluating Atmospheric Mechanisms of the Pattern Effect

Here we evaluate the relative roles of WC strength and tropospheric stability in mediating the pattern effect in the CAM6 patch ensemble and in interannual variability over the historical period. As described in the introduction, tropospheric stability, particularly nonlocal tropospheric stability, has been the prevailing mechanism in the literature, but a thorough comparison has not been conducted.

4.1. CAM6 Patch Ensemble

To evaluate the mechanisms in the CAM6 patch ensemble we use one metric to represent each mechanism and calculate each metric in each patch experiment. We then determine the sensitivity of that metric to the imposed, local SST change ∂metric/∂SST using the same Green's function approach as Section 3. The resulting maps are shown in Figure 3. Each map describes the impact of the imposed SST change at that location on the given metric. In Figure 3, we evaluate the mechanisms using the default metrics described in Section 2.3, that is, WC strength is measured by ψ_{500} (Figure 3b) and the tropospheric stability is measured by CII (Figure 3d). Additionally, we also measure tropospheric stability using LTS (Figure 3c). We further decompose the tropospheric stability mechanism into its local and nonlocal contributions as measured with both LTS and CII (Figures 3e–3h). In Figure 3, the local and nonlocal stability inversion mechanism contributions do not exactly sum to tropospheric stability mechanism (i.e., panels e and g do not sum to panel c and panels f and h do not sum to panel d) because we use different regions of averaging. We average the nonlocal metrics over all oceanic regions between 60°S and 60°N and we average the local metrics only over oceanic subsidence regions between 60°S and 60°N, to be more consistent with underlying theory. To evaluate the metrics, we compute uncentered area-weighted pattern correlations, which we denote r_p. The uncentered metric captures both pattern similarity and differences in magnitude. We interpret a high r_p between $\partial R/\partial$SST and ∂metric/∂SST as evidence that a mechanism mediates the pattern effect over much of the globe.

Figure 3 indicates that the stability mechanism, particularly the nonlocal component, has similar sensitivity to $\partial R/\partial$SST in CAM6. More specifically, ∂LTS/∂SST and ∂CII/∂SST (Figures 3c and 3d) closely resemble $\partial R/\partial$SST (Figure 3a) with r_p values of 0.79 and 0.66, respectively. Further, Figures 3e–3h suggests that the strong positive sensitivity in convective regions is related to changes in nonlocal stability while the negative sensitivity in subsidence regions is largely related to changes in local stability. The nonlocal tropospheric stability sensitivity map has $r_p = 0.80$ when $-\theta_{700}$ (LTS) is used and $r_p = 0.82$ when $-h^*_{500}$ (CII) is used. The local tropospheric stability sensitivity map has $r_p = -0.16$ when θ_s (LTS) is used and $r_p = -0.30$ when h^*_0 (CII) is used. Meanwhile, the WC is sensitive to warming in the tropical Pacific region (Figure 3b) with $r_p = 0.48$ as compared with $\partial R/\partial$SST. We will further evaluate the sensitivity of these values to choice of metric in Section 5.

Next, we estimate of the role of each mechanism using a multivariable ordinary least squares (OLS) regression:

$$\frac{\partial R}{\partial \mathrm{SST}} \approx b_{\mathrm{WC}}\frac{\partial \mathrm{WC}}{\partial \mathrm{SST}} + b_{\mathrm{local}}\frac{\partial \mathrm{local}}{\partial \mathrm{SST}} + b_{\mathrm{nonlocal}}\frac{\partial \mathrm{nonlocal}}{\partial \mathrm{SST}}, \tag{5}$$

where b_i denotes regression coefficients. When measured using the default metrics, the pattern correlation r_p between WC strength and local stability is 0.03, the pattern correlation between WC strength and nonlocal stability is 0.13, and the pattern correlation between local and nonlocal stability is −0.66. Nonetheless, there is little sensitivity of our results to using OLS regression as compared with regularized regression, so we present OLS regression results here. In solving Equation 5 we rescale the predictors to have zero mean and unit variance and we force the intercept to be 0. Multiplying ∂metric/∂SST by its respective regression coefficient b_{metric} yields an estimate of the contribution of each mechanism to the pattern effect. The resulting estimates are shown in Figures 4c–4e, and are proportional to their Jacobian in Figures 3b, 3f, and 3h by construction. In this analysis, we evaluate r_p, which, in Figure 4, is the same as Figure 3 and Table 1 by construction. We also calculate the root mean square error (RMSE) and compare values across the three mechanisms, with lower values indicating a closer relationship between the given mechanism and the pattern effect.

Similar to Figures 3 and 4 shows that the nonlocal stability inversion mechanism is highly correlated with $\partial R/\partial$SST($r_p = -0.82$) and has the lowest RMSE of the three mechanisms. The nonlocal stability inversion mechanism operates predominantly in deep convective regions, which is where $\partial R/\partial$SST is has the largest

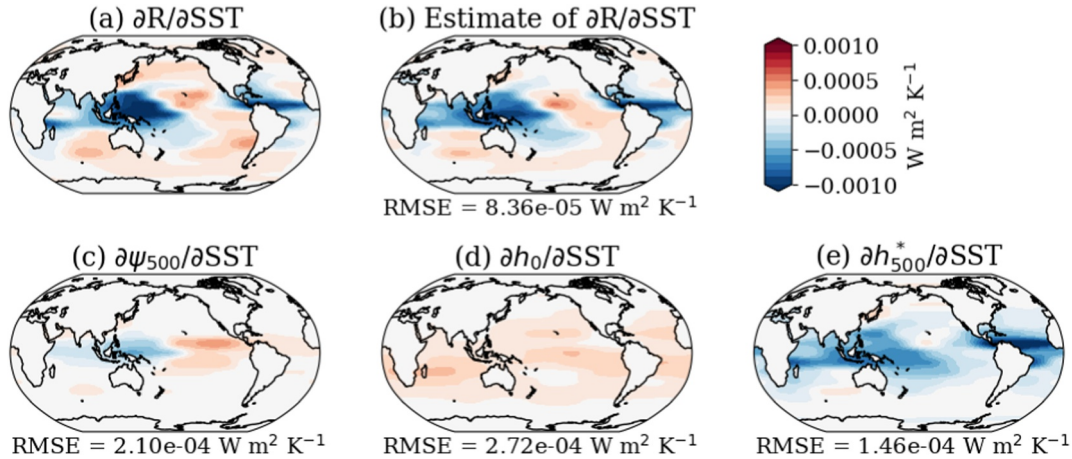


Figure 4. (a) Sensitivity of global-mean total radiative response per degree of grid-box sea-surface temperature warming ($\partial R/\partial$SST, W m^{-2} K^{-1}) (same as Figures 1a and 3a). (b) Estimate of $\partial R/\partial$SST from the multivariable ordinary least squares regression of Equation 5 and contributions from the response of (c) Walker circulation strength, (d) the local stability inversion mechanism, and (e) the nonlocal stability inversion mechanism. Root mean square error values are in comparison to $\partial R/\partial$SST (panel a). Note that the magnitude is resolution dependent and therefore may not easily compare with results from other models.

magnitude. The local stability inversion mechanism tends to contribute to positive $\partial R/\partial$SST, especially in low-cloud regions with $r_p = -0.30$. Finally, there is also a role of WC strength in the deep tropical Pacific, although we will see in Section 5 that this is not robust. The sensitivity maps for the local and nonlocal stability mechanisms (Figures 4d and 4e) are insensitive to the inclusion of WC strength in the model. In the following subsections, we will repeat this analysis for the total cloud feedback and the tropical marine low-cloud feedback. Pattern

Table 1
Pattern Correlation r_p Between $\partial R/\partial$SST and ∂metric/∂SST for Each Metric Described in Section 2.3

Mechanism	Metric	Pattern correlation (r_p)	Local stability	Nonlocal stability
Walker circulation strength	$\overline{\omega}_{e-w}$	0.01		
	$-\psi_{500}$	**0.48**		
Stability	–LTS 30°S–30°N, ocean	0.71		0.77
	–LTS 60°S–60°N, ocean	0.85		0.80
	–LTS 30°S–30°N, ocean subsidence	0.66	−0.23	0.65
	–LTS 60°S–60°N, ocean subsidence	0.79	−0.16	0.73
	–EIS 30°S–30°N, ocean	0.62		0.77
	–EIS 60°S–60°N, ocean	0.81		0.80
	–EIS 30°S–30°N, ocean subsidence	0.48	−0.30	0.65
	–EIS 60°S–60°N, ocean subsidence	0.65	−0.28	0.73
	–ECTEI 30°S–30°N, ocean	0.35		0.73
	–ECTEI 60°S–60°N, ocean	0.73		0.78
	–ECTEI 30°S–30°N, ocean subsidence	0.46	−0.31	0.61
	–ECTEI 60°S–60°N, ocean subsidence	0.65	−0.31	0.68
	CII 30°S–30°N, ocean	0.65		0.79
	CII 60°S–60°N, ocean	0.81		**0.82**
	CII 30°S–30°N, ocean subsidence	0.54	−0.31	0.64
	CII 60°S–60°N, ocean subsidence	0.66	**−0.30**	0.69

Note. Default specifications are bolded. For the stability metrics, the correlation for the total metric is in the left-most column, and the correlation for the nonlocal and local components are in the two right columns.

21698996, 2026, 22, Downloaded from https://agupubs.onlinelibrary.wiley.com/doi/10.1029/2026JD047998 by Schweizerische Akademie Der Medizinischen Wissenschaften (Samw), Wiley Online Library on [21/11/2026]. See the Terms and Conditions (https://onlinelibrary.wiley.com/terms-and-conditions) on Wiley Online Library for rules of use; OA articles are governed by the applicable Creative Commons License

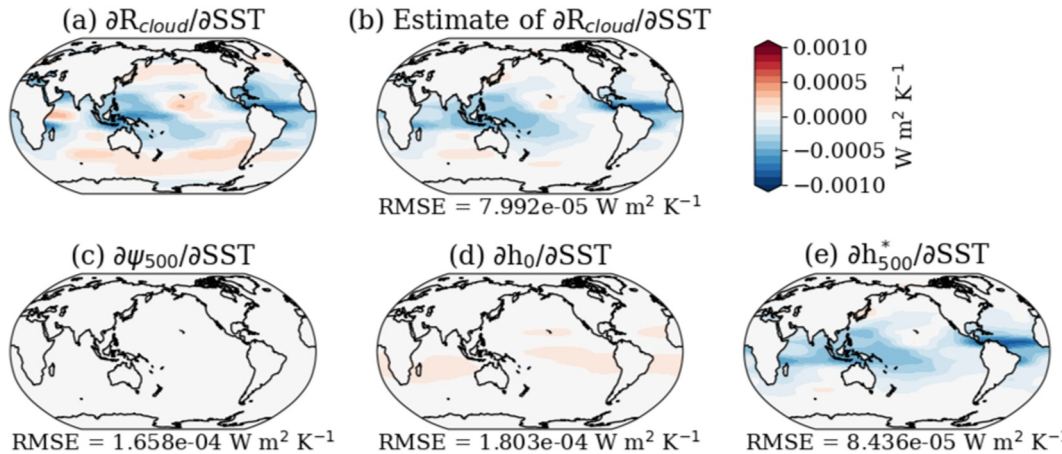


Figure 5. Same as Figure 4 except using ΔR_{cloud} instead of ΔR. Each metric's sensitivity map is multiplied by its regression coefficient, so all panels have the same units. Root mean square error values are in comparison to $\partial R_{\text{cloud}}/\partial$SST (panel a).

correlations r_p between each component of the total feedback and each of the three mechanisms are plotted in Table S1 in Supporting Information S1.

4.1.1. Mechanisms of the Total Cloud Feedback

The theories underlying the proposed mechanisms point largely to their influences on clouds. Further, Figure 1 reveals that $\partial R/\partial$SST is very closely related to $\partial R_{\text{cloud}}/\partial$SST. Here we investigate the sensitivity of the cloud feedback to the pattern of warming. Figure 5 repeats the regression analysis of Section 4.1 using $\partial R_{\text{cloud}}/\partial$SST instead of $\partial R/\partial$SST. The results are shown in Figure 5. Figure 5 indicates that, similar to $\partial R/\partial$SST, $\partial R_{\text{cloud}}/\partial$SST is mediated largely by the nonlocal stability inversion mechanism, as represented by $-h^*_{500}$, $(r_p = 0.88)$ and has the lowest RMSE value of the three mechanisms. On the other hand, Figure 5 indicates little role of WC strength with $r_p = 0.18$ using $-\psi_{500}$. To the extent that WC strength mediates the pattern effect, it is not predominantly operating via cloud feedbacks. In fact, WC strength is more correlated with noncloud feedbacks $(r_p = 0.58)$ and especially the lapse-rate feedback $(r_p = 0.53)$. Further, Figure 5 shows a role of local stability in subsidence regions, with $r_p = -0.49$ when measured using h_0. However, it has the highest RMSE value of the three mechanisms because it does not operate in the deep convective regions, where the pattern effect is strongest.

4.1.2. Mechanisms of the Tropical Marine Low-Cloud Feedback

The single most dominant component of the total cloud feedback is the tropical marine low-cloud feedback (Figure 2). Further, tropical marine low clouds are key to the theories underlying the nonlocal stability inversion mechanism. Here we further investigate the sensitivity of the tropical marine low-cloud feedback to the pattern of warming. We repeat the OLS regression analysis of Section 4.1 using the tropical marine low-cloud component of $\partial R_{\text{cloud}}/\partial$SST, which we call $\partial R_{\text{TropMarineLo}}/\partial$SST, instead of $\partial R/\partial$SST. The results are shown in Figure 6. Much like $\partial R_{\text{cloud}}/\partial$SST, Figure 6 indicates little role of WC strength with $r_p = 0.01$. The tropical marine low-cloud feedback is again dominated by the nonlocal stability inversion mechanism, with $r_p = 0.88$ and the lowest RMSE when measured using $-h^*_{500}$. Overall, Figure 6 suggests that the *nonlocal* stability inversion mechanism is mediating the sensitivity of the tropical marine low-clouds to SST in CAM6.

Recall that the nonlocal stability inversion mechanism describes warming in deep convective regions as influencing low clouds nonlocally. The results of this section are highly consistent with this model of the atmosphere, with warming in deep convective regions having a stabilizing influence via clouds in tropical marine subsidence regions. This nonlocal stability model of the atmosphere is also consistent with a dominant role of the tropical marine low-cloud feedback component in the total cloud feedback with sensitivity to warming in regions of deep convection, as shown in Section 3.

21698996, 2026, 22, Downloaded from https://agupubs.onlinelibrary.wiley.com/doi/10.1029/2026JD047998 by Schweizerische Akademie Der Medizinischen Wissenschaften (Samw), Wiley Online Library on [21/11/2026]. See the Terms and Conditions (https://onlinelibrary.wiley.com/terms-and-conditions) on Wiley Online Library for rules of use; OA articles are governed by the applicable Creative Commons License

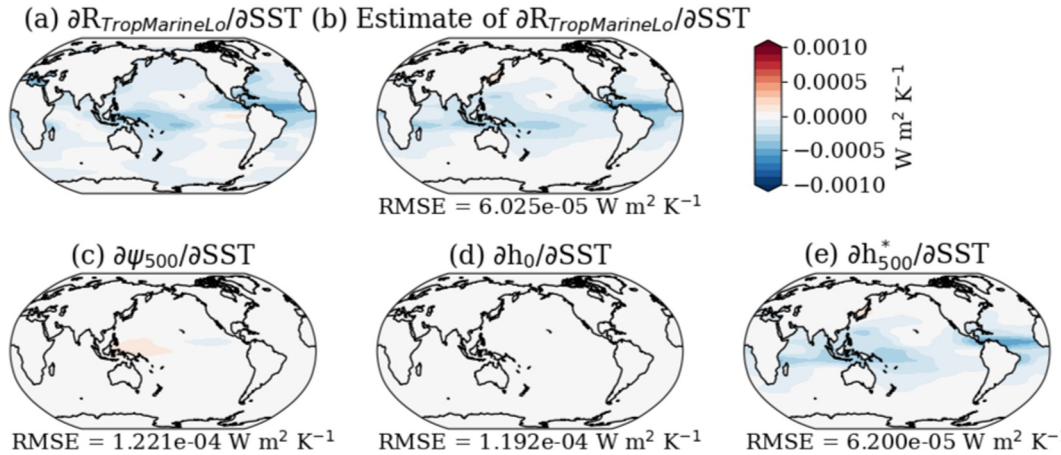


Figure 6. Same as Figure 4 except using the tropical marine low-cloud component of ΔR_{cloud} instead of ΔR. Each metric's sensitivity map is multiplied by its regression coefficient, so all panels have the same units. Root mean square error values are in comparison to $\partial R_{\text{TropMarineLo}}/\partial$SST (panel a).

4.2. Historical Period

The analysis of the previous section is limited to one AGCM– CAM6– and therefore the results are subject to any biases that CAM6 may have. Therefore, we evaluate the three proposed mechanisms of the pattern effect in observations and reanalysis. We use interannual variability over the historical period to evaluate the relationships between (a) SST and each proposed mechanism ∂metric$/\partial$SST and (b) each proposed mechanism and the radiative response $\partial R/\partial$metric. Both relationships must be strong for a mechanism to be a plausible mediator of the pattern effect. This differs from the analysis of the CAM6 patch ensemble of Section 4.1 in both the forcing (patches vs. historical climate) and the type of data (model vs. reanalysis and observations). Therefore, for comparison, we also evaluate the CAM6 historical experiment. The difference between CAM6 historical and observations/reanalysis isolates the influence of model biases and the difference between CAM6 historical and the patch experiments isolates the influence of differing forcings and practical differences in using the Green's function approach in CAM6 but not in the historical period analysis. We note that, unlike the patch experiments, we cannot causally attribute any response to the SST variability. In total, we evaluate the relationships between SST, mechanisms, and radiation over the historical period in three data sets:

1. CAM6 historical, 1979–2014, plotted in blue;
2. ERA5 only, 1979–2022, plotted in green; and
3. A combination of observations and ERA5 reanalysis, various time periods, plotted in pink. In evaluating the relationship between each proposed mechanism and radiative response, we use CERES for radiation and ERA5 to calculate the mechanism metrics from 2001 to 2022, consistent with the CERES record. In evaluating the relationship between SST and each proposed mechanism, we use SST from NOAA NCEP OI SST for SST and ERA5 to calculate mechanism metrics from 1982 to 2022, consistent with the OISST record.

All quantities are linearly detrended to approximately remove the forced response and focus on interannual variability, denoted X'. We show results in the main text using the radiative response $\Delta R'$ as calculated in Kramer et al. (2021). However, due to the approximate nature of the decomposition of Kramer et al. (2021) in calculating $\Delta R'$, we also show the results of this section using the detrended TOA radiative imbalance $\Delta N'$ in Figures S8 and S9 in Supporting Information S1. For this analysis, we calculate a centered Pearson correlation coefficient between timeseries' of annual mean values and denote it r.

The relationship between each of the three mechanisms and the radiative response in interannual variability over the historical period is shown in Figures 7a–7c using $\Delta R'$ and Figures S8a–S8c in Supporting Information S1 using $\Delta N'$. There is general agreement between the CAM6 historical simulations and ERA5 and ERA5/CERES. In all three data sets, the anomaly in radiative response is correlated with the nonlocal tropospheric stability mechanism, but only weakly correlated with WC strength and local stability inversion mechanism. This finding is robust to different methodological choices (Table 2). Even though the correlation coefficients r are comparable

21698996, 2026, 22, Downloaded from https://agupubs.onlinelibrary.wiley.com/doi/10.1029/2026JD047998 by Schweizerische Akademie Der Medizinischen Wissenschaften (Samw), Wiley Online Library on [21/11/2026]. See the Terms and Conditions (https://onlinelibrary.wiley.com/terms-and-conditions) on Wiley Online Library for rules of use; OA articles are governed by the applicable Creative Commons License

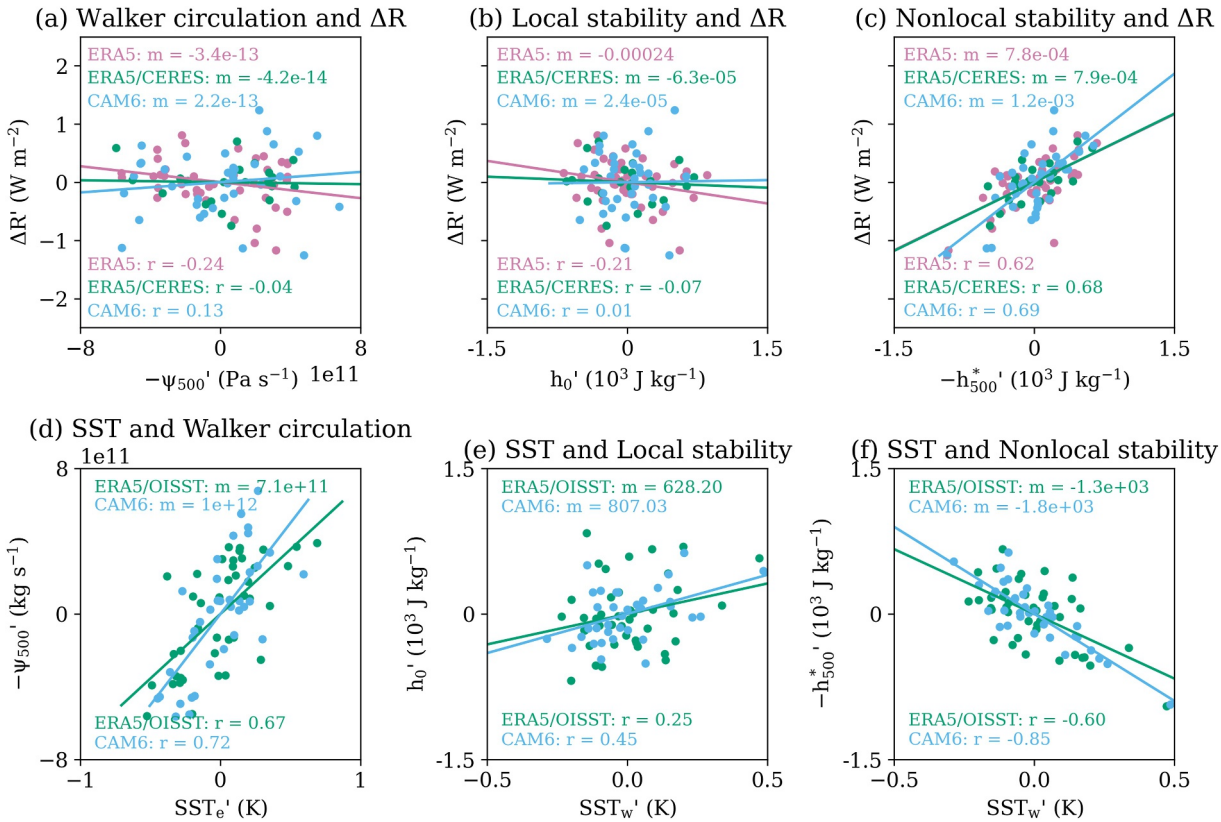


Figure 7. Interannual variability in the radiative response ($\Delta R'$) as a function of interannual variability in (a) Walker circulation (WC) strength, (b) local tropospheric stability, and (c) nonlocal tropospheric stability. In panels (a)–(c), relationships are evaluated in ERA5 from 1979 to 2022 (pink), CERES for radiation and ERA5 for mechanisms from 2001 to 2022 (green), and in CAM6 historical from 1979 to 2014 (blue). Interannual variability in (d) WC strength, (e) local tropospheric stability, and (f) nonlocal tropospheric stability as a function of interannual variability in west Pacific sea-surface temperature. In panels (d)–(f), relationships are evaluated in ERA5 for mechanisms and OISST from 1982 to 2022 (green) and in CAM6 from 1979 to 2014 (blue). All fields on all panels are detrended, as denoted by $(\cdot)'$.

across all three data sets, the slope of the fit line between the nonlocal tropospheric stability mechanism and $\Delta R'$ is steeper in CAM6 historical than in ERA5 and ERA5/CERES, indicating a somewhat stronger relationship in CAM6 than in observations and reanalysis. The results are similar when $\Delta N'$ is used in place of $\Delta R'$ (Figure S8 in Supporting Information S1).

The relationships between SST and each of the three mechanisms in interannual variability over the historical period are shown in Figures 7d–7f. More specifically, we look at interannual variability in SST over the tropical west Pacific between 30°S and 30°N and 80°E and 160°E (SST_w). However, WC strength is more correlated with interannual variability in east Pacific SST (30°N and 200°E and 280°E; SST_e), so we plot SST_e on the x-axis of Figure 7f. The relatively large r values shown in Figures 7d–7f indicate that all three mechanisms are responding to interannual variability in some aspect of the SST pattern.

Overall, despite the difference in forcing (interannual variability over the historical period in lieu of SST patches), the results of this analysis are broadly consistent with the results from the CAM6 patch ensemble, with the nonlocal tropospheric stability mechanism dominating the relationship between the pattern of warming and radiative response. Further, we learn that WC strength is indeed responding to variations in SST, but that variations in WC strength are not correlated with variations in the radiative response. We will evaluate this further in Section 6.

5. Sensitivity to Choice of Metric

Numerous metrics of tropospheric stability have been identified. Here we evaluate the four metrics introduced in Section 2.3: LTS, EIS, estimated cloud-top inversion index (ECTEI), and convective instability (CII). We also compare our default metric for WC strength ψ_{500} with a vertical-velocity based metric $\overline{\omega}_{e-w}$, as described in Section 2.3.

21698996, 2026, 22, Downloaded from https://agupubs.onlinelibrary.wiley.com/doi/10.1029/2026JD047998 by Schweizerische Akademie Der Medizinischen Wissenschaften (Samw), Wiley Online Library on [21/11/2026]. See the Terms and Conditions (https://onlinelibrary.wiley.com/terms-and-conditions) on Wiley Online Library for rules of use; OA articles are governed by the applicable Creative Commons License

21698996, 2026, 22, Downloaded from https://agupubs.onlinelibrary.wiley.com/doi/10.1029/2026JD047998 by Schweizerische Akademie Der Medizinischen Wissenschaften (Samw), Wiley Online Library on [21/11/2026]. See the Terms and Conditions (https://onlinelibrary.wiley.com/terms-and-conditions) on Wiley Online Library for rules of use; OA articles are governed by the applicable Creative Commons License

Table 2
Centered Pearson Correlation Coefficient r for the Metrics Described in Section 2.3

		CAM6			ERA5			ERA5/CERES		
Mechanism	Metric	Total	Local	Nonlocal	Total	Local	Nonlocal	Total	Local	Nonlocal
WC strength	$\overline{\omega}_{e-w}$	0.11			−0.28			0.19		
	$-\psi_{500}$	**0.13**			**−0.24**			**−0.04**		
Stability	–LTS 30°S–30°N, ocean	0.69		0.54	0.61		0.56	0.83		0.59
	–LTS 60°S–60°N, ocean	0.80		0.62	0.60		0.54	0.88		0.69
	–LTS 30°S–30°N, ocean subs	0.74	0.00	0.52	0.61	−0.22	0.54	0.90	0.00	0.60
	–LTS 60°S–60°N, ocean subs	0.80	0.01	0.58	0.59	−0.19	0.51	0.92	−0.01	0.66
	–EIS 30°S–30°N, ocean	0.75		0.55	0.67		0.55	0.65		0.59
	–EIS 60°S–60°N, ocean	0.83		0.62	0.71		0.53	0.66		0.69
	–EIS 30°S–30°N, ocean subs	0.73	0.04	0.53	0.59	−0.15	0.53	0.67	−0.03	0.60
	–EIS 60°S–60°N, ocean subs	0.79	0.04	0.59	0.63	−0.13	0.51	0.71	−0.06	0.66
	–ECTEI 30°S–30°N, ocean	0.62		0.49	0.38		0.46	0.34		0.49
	–ECTEI 60°S–60°N, ocean	0.70		0.57	0.43		0.45	0.35		0.61
	–ECTEI 30°S–30°N, ocean subs	0.65	0.03	0.40	0.39	−0.17	0.46	0.43	−0.04	0.44
	–ECTEI 60°S–60°N, ocean subs	0.72	0.03	0.49	0.44	−0.15	0.44	0.47	−0.07	0.52
	CII, 30°S–30°N ocean	0.79		0.62	0.69		0.64	0.69		0.59
	CII, 60°S–60°N ocean	0.86		**0.69**	0.64		**0.62**	0.65		**0.68**
	CII, 30°S–30°N ocean subs	0.77	0.02	0.61	0.59	−0.22	0.63	0.70	−0.04	0.59
	CII, 60°S–60°N ocean subs	0.81	**0.01**	0.66	0.59	**−0.21**	0.61	0.70	**−0.07**	0.64

Note. All metrics and ΔR are detrended and annually averaged. Default specifications are bolded. Results are shown for the CAM6 historical experiment, ERA5 from 1979 to 2022, and using a combination of ERA5 and observations from 2001 to 2022, as described in Section 4.2.

5.1. CAM6 Patch Ensemble

The metrics chosen to represent each mechanism are merely proxies; there are numerous metrics which could reasonably be used to represent each mechanism. We first evaluate the sensitivity to the choice of metric by computing r_p values using the patterns of ∂metric/∂SST and $\partial R/\partial$SST for each choice of metric described in Section 2.3 (Table 1). Table 1 reveals that the nonlocal stability inversion mechanism is highly correlated with the pattern effect, regardless of the choice of metric or region of averaging. The r_p values range from 0.61 to 0.82. For the nonlocal tropospheric stability mechanism, r_p is higher when the metric is averaged over 60°S–60°N than over 30°S–30°N. The latter highlights the strong role of midlatitude clouds in the tropospheric stability mechanism in CAM6. There is not much sensitivity to using LTS, EIS, ECTEI, or CII except that correlations are slightly lower in magnitude for ECTEI than for other metrics. On the other hand, there is a smaller relationship between the local stability inversion mechanism and the pattern effect using any metric, with r_p values ranging from −0.16 to −0.31. Finally, WC strength has a larger magnitude correlation with the pattern effect when measured using $-\psi_{500}$ than when measured using $\overline{\omega}_{e-w}$, indicating that this relationship is not robust.

In order to further evaluate each metric and, more generally, the robustness of the results in Section 4, we adapt and invoke a "specification" or "multiverse" analysis, which is commonly used in the social sciences (Simonsohn et al., 2020; Steegen et al., 2016). In general, specification analyses are used to evaluate the sensitivity of statistical results to methodological choices by the researchers by creating many versions of the statistical model, each with a different set of "specifications." Here, we use a specification analysis to present the sensitivity of our results to the choice of metric of WC strength, local stability inversion, and nonlocal stability inversion. We evaluate local stability metrics—LTS, EIS, ECTEI, and CII—over oceanic subsidence regions between 60°S and 60°N and nonlocal stability metrics over all oceanic regions between 60°S and 60°N. We also evaluate the two measures of WC strength: ψ_{500} and $\overline{\omega}_{e-w}$. We calculate the multivariable OLS regression coefficients using each

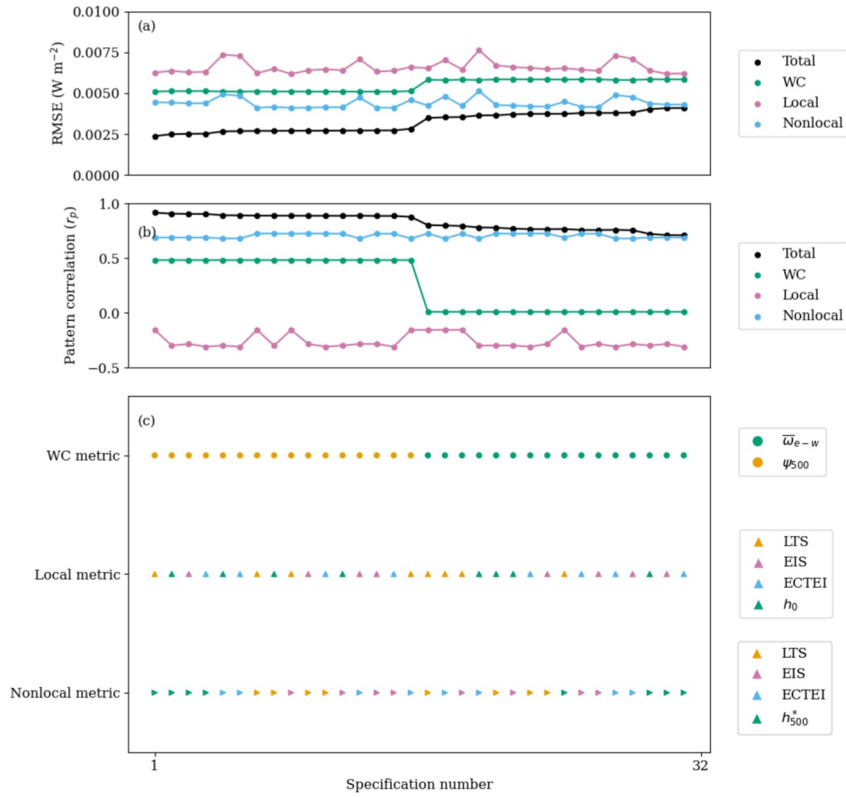


Figure 8. (a) Root mean square error (RMSE) of $\partial R/\partial$SST as estimated in Equation 5 as compared with $\partial R/\partial$SST simulated in CAM6 for each patch experiment, sorted from lowest to highest (black). RMSE of the contribution of each term in Equation 5 as compared with $\partial R/\partial$SST simulated in CAM6 for each patch experiment (colors). (b) Uncentered pattern correlation r_p between $\partial R/\partial$SST as estimated in Equation 5 and $\partial R/\partial$SST for various specifications of the model in Equation 5 (black). Uncentered pattern correlation r_p between each term in Equation 5 and $\partial R/\partial$SST for various specifications of the model in Equation 5 (colors). (c) Specifications used for Equation 5. The data on all three panels are sorted by model skill (RMSE), as in panel (a).

metric for a total of $2 \times 4 \times 4 = 32$ "specifications." For visual clarity, we do not evaluate the sensitivity to region of averaging of stability metrics in this section, but the r_p values are available in Table 1.

For each specification, we solve Equation 5 to yield an estimate of $\partial R/\partial$SST. The terms on the right-hand side of Equation 5 estimate the contributions of each mechanism. We evaluate the skill of each version of the regression model by calculating the root-mean squared error (RMSE) and pattern correlation (r_p) between $\partial R/\partial$SST and its estimate. We further evaluate the contribution of each of the three mechanisms by calculating the RMSE and r_p values between $\partial R/\partial$SST and each mechanism's contribution (Figures 8a and 8b). The r_p values between $\partial R/\partial$SST and each mechanism's contribution are the same values as in Table 1 by construction. In Figure 8, the results are sorted by model skill with the most skillful model on the left, as measured using the RMSE between $\partial R/\partial$SST and its estimate.

Examining Figure 8 reveals that nonlocal stability robustly has a high-magnitude correlation and low RMSE when compared with $\partial R/\partial$SST. There is little sensitivity to use of LTS, EIS, ECTEI, or CII. On the other hand, local stability has a robustly lower-magnitude correlation and higher RMSE when compared with $\partial R/\partial$SST. WC strength is sensitive to choice of metric. These findings are consistent with the r_p values in Table 1.

5.2. Historical Period

We also evaluate the sensitivity of our historical period results (Section 4.2) to choice of metric. Table 2 shows the centered Pearson correlation coefficient r between $\partial R/\partial$SST and each mechanism for the same variety of metrics

21698996, 2026, 22, Downloaded from https://agupubs.onlinelibrary.wiley.com/doi/10.1029/2026JD047998 by Schweizerische Akademie Der Medizinischen Wissenschaften (Samw), Wiley Online Library on [21/11/2026]. See the Terms and Conditions (https://onlinelibrary.wiley.com/terms-and-conditions) on Wiley Online Library for rules of use; OA articles are governed by the applicable Creative Commons License

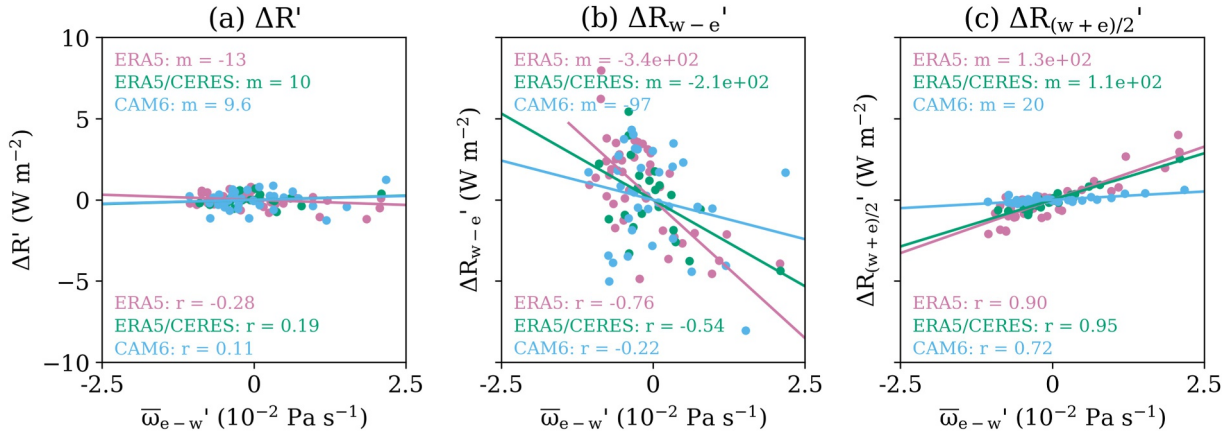


Figure 9. Interannual variability (a) global-mean radiative response ($\Delta R'$), (b) Walker circulation (WC)-linked radiative response, and (c) net WC-region radiative response as a function of interannual variability in WC strength. Relationships are evaluated in ERA5 from 1979 to 2022 (pink), CERES for top-of-atmosphere radiation and ERA5 for WC strength from 2001 to 2022 (green), and in CAM6 historical from 1979 to 2014 (blue). All fields on all panels are detrended, as denoted by $(\cdot)'$.

as in Table 1 using the CAM6 historical experiments, ERA5 reanalysis, and a combination of ERA5 reanalysis and CERES observations as described in Section 4.2. Table 2 reveals that the higher-magnitude r values for nonlocal stability and lower-magnitude r values for WC strength and local stability are robust across metrics. Further, when the nonlocal stability mechanism is measured with ECTEI, r values are consistently lower magnitude than when measured using LTS, EIS, or CII.

Overall, the robustness analysis using the CAM6 patch ensemble (Figure 8 and Table 1) and the robustness analysis using the historical period (Table 2) agree that nonlocal stability is a robustly correlated with the pattern effect. However, ECTEI is somewhat less correlated than the other metrics, especially over the historical period. Meanwhile, local stability has a lower but nonzero correlation with the pattern effect across data sets. Further, while the decomposition of Figure 4 indicates some role of WC strength, this result is not robust and does not hold up over the historical period. We will further evaluate the (lack of) role of WC strength in the next section.

6. Why Not Walker Circulation Strength?

While WC strength has not received as much attention as tropospheric stability as a mediator of the pattern effect, it is known to be closely tied to the tropical Pacific zonal SST gradient. Further, variations in WC strength are linked with variations in local TOA radiation (Duffy & O'Gorman, 2023). Indeed, WC strength varies with the SST anomalies in the CAM6 patch experiments (Figure 3b) and varies with SST anomalies during the historical period in observations/reanalysis (Figure 7f). However, these variations in WC strength over the historical period are not correlated with changes in global-mean radiative response, which seems inconsistent with our a priori expectation. To further evaluate the impact of variations in WC strength on the radiative response, we compare changes in global-mean radiative response with the portion of the radiative response which is colocated with the WC in Figure 9 (and Figure S9 in Supporting Information S1 using $\Delta N'$). Figure 9 compares the relationship between WC strength, as measured using differences in $\overline{\omega}_{e-w}$, and radiative response in interannual variability for three "flavors" of radiative response:

- global-mean radiative response (ΔR), which is relevant to the pattern effect;
- WC-linked radiative response, defined as the difference in ΔR between the west Pacific and east Pacific (ΔR_{w-e}), which is colocated with the WC when measured using $\overline{\omega}_{e-w}$; and
- net WC-region radiative response, defined as the average of radiative response between the west Pacific and east Pacific $\left(\Delta R_{(w+e)/2}\right)$, which is the net contribution of the WC-linked to global-mean radiative response.

As in Figure 7, we analyze the relationship between WC strength and radiative response using detrended interannual variability over the historical period using ERA5, a combination of ERA5 and CERES, and CAM6 historical simulations. Note that for this analysis, we are using $\overline{\omega}_{e-w}$ instead of our default metric, ψ_{500}, because it has distinct west and east Pacific boxes which allows us to check for compensating radiative responses in those

21698996, 2026, 22, Downloaded from https://agupubs.onlinelibrary.wiley.com/doi/10.1029/2026JD047998 by Schweizerische Akademie Der Medizinischen Wissenschaften (Samw), Wiley Online Library on [21/11/2026]. See the Terms and Conditions (https://onlinelibrary.wiley.com/terms-and-conditions) on Wiley Online Library for rules of use; OA articles are governed by the applicable Creative Commons License

21698996, 2026, 22, Downloaded from https://agupubs.onlinelibrary.wiley.com/doi/10.1029/2026JD047998 by Schweizerische Akademie Der Medizinischen Wissenschaften (Samw), Wiley Online Library on [21/11/2026]. See the Terms and Conditions (https://onlinelibrary.wiley.com/terms-and-conditions) on Wiley Online Library for rules of use; OA articles are governed by the applicable Creative Commons License

regions. This metric, $\overline{\omega}_{e-w}$, is not correlated with the pattern effect in the CAM6 patch ensemble or over the historical period.

We find that, consistent with previous studies, there is a strong correlation between WC strength and $\Delta R'_{w-e}$ (Figure 9b). We expect that a stronger WC means more high clouds and less outgoing longwave radiation over the west Pacific, and more low clouds and increased reflected SW radiation over the east Pacific, and conversely for a weaker WC. However, to the extent that these west and east Pacific variations compensate one another, we expect a weaker relationship between WC strength and $\Delta R'_{(w+e)/2}$, which is indeed the case (Figure 9c). Further, the interannual variability in $\Delta R'_{(w+e)/2}$ does not significantly contribute to the global-mean $\Delta R'$ (Figures 9a and 9c). Therefore, variations in WC strength indeed affect the local radiative response, but have little influence on global-mean radiative response because of (a) the partial compensation between east and west Pacific radiative responses to changes in WC strength and (b) because of the relatively small geographic influence of WC strength on TOA radiation.

7. Discussion and Conclusions

Here we have undertaken a thorough investigation of the atmospheric mechanisms of the pattern effect.

First, we created an ensemble of patch experiments using CAM6 and used it to decompose $\partial R/\partial$SST into contributions from various types of feedbacks and found that cloud feedbacks dominate. Previous authors have found a role of the lapse-rate feedback, but we found this role to be much smaller when fixed RH kernels are used than when fixed specific-humidity kernels are used. We further decomposed the cloud feedback into contributions for the six assessed cloud feedback contributions of Sherwood et al. (2020). We leveraged the COSP satellite simulator to find a large role of tropical marine low-cloud feedbacks in response to warming in deep convective regions, but not in response to warming in subsidence regions. This is indicative of nonlocal control on tropical marine low-cloud feedbacks, consistent with some previous studies (Alessi & Rugenstein, 2023; Myers et al., 2023).

Next, we evaluated the relative roles of local and nonlocal stability inversion and WC strength in mediating the pattern effect in the CAM6 patch ensemble and over the historical period. We found that the pattern effect is closely related to measures of the nonlocal tropospheric stability inversion mechanism, consistent with Andrews and Webb (2018) and Ceppi and Gregory (2017). Of the many measures of nonlocal stability inversion, LTS, EIS, and the "circus tent" model as represented by CII are all highly correlated with the radiative response and ECTEI is slightly less correlated. Despite our a priori expectation, we found little relationship between WC strength and the pattern effect because the WC strength's impact on the radiative response over the west Pacific and east Pacific largely cancel one another and the radiative impact of the WC strength is local to the tropical Pacific.

In addition to a stronger mechanistic understanding of the pattern effect, that h^*_{500} is highly correlated with the radiative response is meaningful because it may provide a *constraint* on the pattern effect. Model evidence suggests that feedbacks become less negative over time, but disagree on the extent (Dong et al., 2020). Part of this disagreement is due to intermodel spread in the pattern of SST warming, which is highly uncertain and we have not addressed it here (Watanabe et al., 2024; Wills et al., 2022). The rest of the disagreement is due to intermodel spread in the radiative response to a given SST pattern, and the updated understanding that we have provided here has the potential to provide a constraint on uncertainty in the latter. Importantly, the response of tropical-mean h^*_{500} to warming is potentially better constrained than the response of LTS to warming because it is controlled by lapse rates in convectively-active regions for which there is theoretical understanding (e.g., entraining moist adiabat). Therefore, this work lays the groundwork for future work in constraining the magnitude of $\Delta\lambda$.

Conflict of Interest

The authors declare no conflicts of interest relevant to this study.

Availability Statement

Raw data from the CAM6 patch ensemble are available via GDEX at https://gdex.ucar.edu/datasets/d436263 (Duffy, 2026b) and have been submitted to the Green's Function Model Intercomparison Project archive. ERA5 data was downloaded from Copernicus Climate Change Service Climate Data Store (Hersbach et al., 2020, 2023),

CERES EBAF data was downloaded from NASA (NASA/LARC/SD/ASDC, 2022), and NOAA OISST data was downloaded from the NCAR Research Data Archive (National Climatic Data Center, NESDIS, NOAA, U.S. Department of Commerce & National Centers for Environmental Prediction, National Weather Service, NOAA, U.S. Department of Commerce, 1986). Processed data used in this study are available on Zenodo at https://doi.org/10.5281/zenodo.22713324 (Duffy, 2026a).

Acknowledgments

Yue Dong, Jonah Bloch-Johnson, and Bosong Zhang provided helpful guidance in setting up and analyzing the patch experiments. We also thank Andrew Williams, Henri Drake, Shiv Priyam Raghuraman, and the anonymous reviewers for their insightful feedback. This work was funded by NOAA's Modeling, Analysis, Predictions, and Projections (MAPP) Program under Award NA20OAR4310392. Portions of this study were supported by the Regional and Global Model Analysis component of the Earth and Environmental System Modeling Program of the U.S. Department of Energy Office of Biological and Environmental Research under Lawrence Livermore National Laboratory Subaward DE-AC52-07NA27344, Lawrence Berkeley National Laboratory Subaward DE-AC02-05CH11231, and Pacific Northwest National Laboratory Subaward DE-AC05-76RL01830. R. C. J. W. was supported by the Swiss National Science Foundation (Grant PCEFP2-20337). This work was also supported by the NSF National Center for Atmospheric Research (NCAR), a major facility sponsored by the National Science Foundation under Cooperative Agreement No. 1852977. Computing resources were provided by the Climate Simulation Laboratory at NCAR's Computational and Information Systems Laboratory.

References

Alessi, M. J., & Rugenstein, M. A. A. (2023). Surface temperature pattern scenarios suggest higher warming rates than current projections. *Geophysical Research Letters*, *50*(23), e2023GL105795. https://doi.org/10.1029/2023GL105795

Andrews, T., Gregory, J. M., Paynter, D., Silvers, L. G., Zhou, C., Mauritsen, T., et al. (2018). Accounting for changing temperature patterns increases historical estimates of climate sensitivity. *Geophysical Research Letters*, *45*(16), 8490–8499. https://doi.org/10.1029/2018GL078887

Andrews, T., Gregory, J. M., & Webb, M. J. (2015). The dependence of radiative forcing and feedback on evolving patterns of surface temperature change in climate models. *Journal of Climate*, *28*(4), 1630–1648. https://doi.org/10.1175/jcli-d-14-00545.1

Andrews, T., & Webb, M. J. (2018). The dependence of global cloud and lapse rate feedbacks on the spatial structure of tropical Pacific warming. *Journal of Climate*, *31*(2), 641–654. https://doi.org/10.1175/JCLI-D-17-0087.1

Armour, K. C. (2017). Energy budget constraints on climate sensitivity in light of inconstant climate feedbacks. *Nature Climate Change*, *7*(5), 331–335. https://doi.org/10.1038/nclimate3278

Armour, K. C., Bitz, C. M., & Roe, G. H. (2013). Time-varying climate sensitivity from regional feedbacks. *Journal of Climate*, *26*(13), 4518–4534. https://doi.org/10.1175/JCLI-D-12-00544.1

Armour, K. C., Proistosescu, C., Dong, Y., Hahn, L. C., Blanchard-Wrigglesworth, E., Pauling, A. G., et al. (2024). Sea-surface temperature pattern effects have slowed global warming and biased warming-based constraints on climate sensitivity. *Proceedings of the National Academy of Sciences*, *121*(12), e2312093121. https://doi.org/10.1073/pnas.2312093121

Barsugli, J. J., & Sardeshmukh, P. D. (2002). Global atmospheric sensitivity to tropical SST anomalies throughout the Indo-Pacific basin. *Journal of Climate*, *15*(23), 3427–3442. https://doi.org/10.1175/1520-0442(2002)015⟨3427:GASTTS⟩2.0.CO;2

Bloch-Johnson, J., Rugenstein, M. A. A., Alessi, M. J., Proistosescu, C., Zhao, M., Zhang, B., et al. (2024). The Green's Function Model Intercomparison Project (GFMIP) protocol. *Journal of Advances in Modeling Earth Systems*, *16*(2), e2023MS003700. https://doi.org/10.1029/2023MS003700

Bodas-Salcedo, A., Webb, M. J., Bony, S., Chepfer, H., Dufresne, J. L., Klein, S., et al. (2011). COSP: Satellite simulation software for model assessment. *Bulletin of the American Meteorological Society*, *92*(8), 1023–1043. https://doi.org/10.1175/2011BAMS2856.1

Bony, S., & Dufresne, J.-L. (2005). Marine boundary layer clouds at the heart of tropical cloud feedback uncertainties in climate models. *Geophysical Research Letters*, *32*(20), L20806. https://doi.org/10.1029/2005GL023851

Ceppi, P., & Gregory, J. M. (2017). Relationship of tropospheric stability to climate sensitivity and Earth's observed radiation budget. *Proceedings of the National Academy of Sciences*, *114*(50), 13126–13131. https://doi.org/10.1073/pnas.1714308114

Coats, S., & Karnauskas, K. B. (2017). Are simulated and observed twentieth century tropical pacific sea surface temperature trends significant relative to internal variability? *Geophysical Research Letters*, *44*(19), 9928–9937. https://doi.org/10.1002/2017GL074622

Danabasoglu, G., Lamarque, J., Bacmeister, J., Bailey, D. A., DuVivier, A. K., Edwards, J., et al. (2020). The Community Earth System Model Version 2 (CESM2). *Journal of Advances in Modeling Earth Systems*, *12*(2), e2019MS001916. https://doi.org/10.1029/2019MS001916

Dong, Y., Armour, K. C., Zelinka, M. D., Proistosescu, C., Battisti, D. S., Zhou, C., & Andrews, T. (2020). Intermodel spread in the pattern effect and its contribution to climate sensitivity in CMIP5 and CMIP6 models. *Journal of Climate*, *33*(18), 7755–7775. https://doi.org/10.1175/JCLI-D-19-1011.1

Dong, Y., Proistosescu, C., Armour, K. C., & Battisti, D. S. (2019). Attributing historical and future evolution of radiative feedbacks to regional warming patterns using a Green's Function approach: The preeminence of the western Pacific. *Journal of Climate*, *32*(17), 5471–5491. https://doi.org/10.1175/JCLI-D-18-0843.1

Duffy, M. L. (2026a). Atmospheric mechanisms of the pattern effect [Dataset]. *Zenodo*. https://doi.org/10.5281/zenodo.22713324

Duffy, M. L. (2026b). CAM6 SST patch ensemble [Dataset]. *NSF National Center for Atmospheric Research*. https://doi.org/10.5065/K1Y2-YE23

Duffy, M. L., & O'Gorman, P. A. (2023). Intermodel spread in Walker circulation responses linked to spread in moist stability and radiation responses. *Journal of Geophysical Research: Atmospheres*, *128*(1), e2022JD037382. https://doi.org/10.1029/2022JD037382

Eidhammer, T., Gettelman, A., Thayer-Calder, K., Watson-Parris, D., Elsaesser, G., Morrison, H., et al. (2024). An extensible perturbed parameter ensemble for the Community Atmosphere Model version 6. *Geoscientific Model Development*, *17*(21), 7835–7853. https://doi.org/10.5194/gmd-17-7835-2024

Espy, J. P. (1836). Essays on meteorology. No. IV. *Journal of the Franklin Institute*, *22*(4), 239–246. https://doi.org/10.1016/S0016-0032(36)91215-2

Gregory, J. M., Andrews, T., & Good, P. (2015). The inconstancy of the transient climate response parameter under increasing CO_2. *Philosophical Transactions of the Royal Society A*, *373*(2054), 20140417. https://doi.org/10.1098/rsta.2014.0417

Held, I. M., & Shell, K. M. (2012). Using relative humidity as a state variable in climate feedback analysis. *Journal of Climate*, *25*(8), 2578–2582. https://doi.org/10.1175/JCLI-D-11-00721.1

Hersbach, H., Bell, B., Berrisford, P., Biavati, G., Horányi, A., Muñoz-Sabater, J., et al. (2023). ERA5 monthly averaged data on pressure levels from 1940 to present [Dataset]. *Copernicus Climate Change Service (C3S) Climate Data Store (CDS)*. https://doi.org/10.24381/CDS.6860A573

Hersbach, H., Bell, B., Berrisford, P., Hirahara, S., Horányi, A., Muñoz-Sabater, J., et al. (2020). The ERA5 global reanalysis. *Quarterly Journal of the Royal Meteorological Society*, *146*(730), 1999–2049. https://doi.org/10.1002/qj.3803

Hu, X., Yang, S., & Cai, M. (2016). Contrasting the eastern Pacific El Niño and the central Pacific El Niño: Process-based feedback attribution. *Climate Dynamics*, *47*(7–8), 2413–2424. https://doi.org/10.1007/s00382-015-2971-9

Huang, B., Liu, C., Banzon, V., Freeman, E., Graham, G., Hankins, B., et al. (2021). Improvements of the Daily Optimum Interpolation Sea Surface Temperature (DOISST) version 2.1. *Journal of Climate*, *34*(8), 2923–2939. https://doi.org/10.1175/JCLI-D-20-0166.1

Huang, H., & Huang, Y. (2023). Radiative sensitivity quantified by a new set of radiation flux kernels based on the ECMWF reanalysis v5 (ERA5). *Earth System Science Data*, *15*(7), 3001–3021. https://doi.org/10.5194/essd-15-3001-2023

21698996, 2026, 22, Downloaded from https://agupubs.onlinelibrary.wiley.com/doi/10.1029/2026JD047998 by Schweizerische Akademie Der Medizinischen Wissenschaften (Samw), Wiley Online Library on [21/11/2026]. See the Terms and Conditions (https://onlinelibrary.wiley.com/terms-and-conditions) on Wiley Online Library for rules of use; OA articles are governed by the applicable Creative Commons License

Janoski, T. P., Mitevski, I., Kramer, R. J., Previdi, M., & Polvani, L. M. (2025). Climkern v1.2: A new python package and kernel repository for calculating radiative feedbacks. *Geoscientific Model Development*, *18*(10), 3065–3079. https://doi.org/10.5194/gmd-18-3065-2025

Kawai, H., Koshiro, T., & Webb, M. J. (2017). Interpretation of factors controlling low cloud cover and low cloud feedback using a unified predictive index. *Journal of Climate*, *30*(22), 9119–9131. https://doi.org/10.1175/JCLI-D-16-0825.1

Klein, S. A., & Hartmann, D. L. (1993). The seasonal cycle of low stratiform clouds. *Journal of Climate*, *6*(8), 1587–1606. https://doi.org/10.1175/1520-0442(1993)006⟨1587:TSCOLS⟩2.0.CO;2

Kosovelj, K., & Zaplotnik, Z. (2023). Indices of Pacific walker circulation strength. *Atmosphere*, *14*(2), 397. https://doi.org/10.3390/atmos14020397

Kramer, R. J., He, H., Soden, B. J., Oreopoulos, L., Myhre, G., Forster, P. M., & Smith, C. J. (2021). Observational evidence of increasing global radiative forcing. *Geophysical Research Letters*, *48*(7), e2020GL091585. https://doi.org/10.1029/2020GL091585

Lee, S., L'Heureux, M., Wittenberg, A. T., Seager, R., O'Gorman, P. A., & Johnson, N. C. (2022). On the future zonal contrasts of equatorial Pacific climate: Perspectives from observations, simulations, and theories. *npj Climate and Atmospheric Science*, *5*(1), 82. https://doi.org/10.1038/s41612-022-00301-2

Mackie, A., Byrne, M. P., Van De Koot, E. K., & Williams, A. I. L. (2025). Circulation and cloud responses to patterned SST warming. *Geophysical Research Letters*, *52*(8), e2024GL112543. https://doi.org/10.1029/2024GL112543

Marvel, K., Pincus, R., Schmidt, G. A., & Miller, R. L. (2018). Internal variability and disequilibrium confound estimates of climate sensitivity from observations. *Geophysical Research Letters*, *45*(3), 1595–1601. https://doi.org/10.1002/2017GL076468

Myers, T. A., Zelinka, M. D., & Klein, S. A. (2023). Observational constraints on the cloud feedback pattern effect. *Journal of Climate*, *36*(18), 6533–6545. https://doi.org/10.1175/JCLI-D-22-0862.1

NASA/LARC/SD/ASDC. (2022). CERES energy Balanced and Filled (EBAF) TOA monthly means data in netCDF edition 4.2 [Dataset]. *NASA Langley Atmospheric Science Data Center DAAC*. https://doi.org/10.5067/TERRA-AQUA-NOAA20/CERES/EBAF-TOA_L3B004.2

National Climatic Data Center, NESDIS, NOAA, U.S. Department of CommerceNational Centers for Environmental Prediction, National Weather Service, NOAA, U.S. Department of Commerce. (1986). NOAA NCEP optimum interpolation sea surface temperature analysis [Dataset]. *Research Data Archive at the National Center for Atmospheric Research, Computational and Information Systems Laboratory*. https://data.ucar.edu/dataset/noaa-ncep-optimum-interpolation-sea-surface-temperature-analysis

Palazzo Corner, S., Siegert, M., Ceppi, P., Fox-Kemper, B., Frölicher, T. L., Gallego-Sala, A., et al. (2023). The zero emissions commitment and climate stabilization. *Frontiers in Science*, *1*, 1170744. https://doi.org/10.3389/fsci.2023.1170744

Pendergrass, A. G., Conley, A., & Vitt, F. M. (2018). Surface and top-of-atmosphere radiative feedback kernels for CESM-CAM5. *Earth System Science Data*, *10*(1), 317–324. https://doi.org/10.5194/essd-10-317-2018

Qin, Y., Zelinka, M. D., & Klein, S. A. (2022). On the correspondence between atmosphere-only and coupled simulations for radiative feedbacks and forcing from CO_2. *Journal of Geophysical Research: Atmospheres*, *127*(3), e2021JD035460. https://doi.org/10.1029/2021JD035460

Quan, H., Zhang, B., Wang, C., & Fueglistaler, S. (2024). Nonlinear radiative response to patterned global warming due to convection aggregation and nonlinear tropical dynamics. *Journal of Climate*, *37*(21), 5675–5686. https://doi.org/10.1175/JCLI-D-23-0539.1

Raghuraman, S. P., & Medeiros, B. (2026). Cloud feedback overestimated in coupled CESM2 simulations relative to AMIP simulations and satellite observations: Importance of the pattern effect and implications for climate sensitivity. *Environmental Research Letters*, *21*(8), 084018. https://doi.org/10.1088/1748-9326/ae5fab

Raghuraman, S. P., Medeiros, B., & Gettelman, A. (2024). Observational quantification of tropical high cloud changes and feedbacks. *Journal of Geophysical Research: Atmospheres*, *129*(7), e2023JD039364. https://doi.org/10.1029/2023JD039364

Randall, D. A., Wood, R. A., Bony, S., Colman, R., Fichefet, T., Fyfe, J., et al. (2007). Cilmate models and their evaluation. In *Climate change 2007: The physical science basis. Contribution of working group I to the fourth assessment report of the intergovernmental panel on climate change*. Cambridge University Press.

Ringer, M. A., Andrews, T., & Webb, M. J. (2014). Global-mean radiative feedbacks and forcing in atmosphere-only and coupled atmosphere-ocean climate change experiments. *Geophysical Research Letters*, *41*(11), 4035–4042. https://doi.org/10.1002/2014GL060347

Rugenstein, M., Bloch-Johnson, J., Gregory, J., Andrews, T., Mauritsen, T., Li, C., et al. (2020). Equilibrium climate sensitivity estimated by equilibrating climate models. *Geophysical Research Letters*, *47*(4), e2019GL083898. https://doi.org/10.1029/2019GL083898

Rugenstein, M., Zelinka, M., Karnauskas, K., Ceppi, P., & Andrews, T. (2023). Patterns of surface warming matter for climate sensitivity. *EOS*, *104*. https://doi.org/10.1029/2023EO230411

Seager, R., Henderson, N., & Cane, M. (2022). Persistent discrepancies between observed and modeled trends in the tropical Pacific Ocean. *Journal of Climate*, *35*(14), 4571–4584. https://doi.org/10.1175/JCLI-D-21-0648.1

Senior, C. A., & Mitchell, J. F. B. (2000). The time-dependence of climate sensitivity. *Geophysical Research Letters*, *27*(17), 2685–2688. https://doi.org/10.1029/2000GL011373

Sherwood, S., Webb, M. J., Annan, J. D., Armour, K. C., Forster, P. M., Hargreaves, J. C., et al. (2020). An assessment of Earth's climate sensitivity using multiple lines of evidence. *Reviews of Geophysics*, *58*(4), e2019RG000678. https://doi.org/10.1029/2019RG000678

Simonsohn, U., Simmons, J. P., & Nelson, L. D. (2020). Specification curve analysis. *Nature Human Behaviour*, *4*(11), 1208–1214. https://doi.org/10.1038/s41562-020-0912-z

Soden, B. J., Held, I. M., Colman, R., Shell, K. M., Kiehl, J. T., & Shields, C. A. (2008). Quantifying climate feedbacks using radiative kernels. *Journal of Climate*, *21*(14), 3504–3520. https://doi.org/10.1175/2007JCLI2110.1

Steegen, S., Tuerlinckx, F., Gelman, A., & Vanpaemel, W. (2016). Increasing transparency through a multiverse analysis. *Perspectives on Psychological Science*, *11*(5), 702–712. https://doi.org/10.1177/1745691616658637

Stevens, B., Sherwood, S. C., Bony, S., & Webb, M. J. (2016). Prospects for narrowing bounds on earth's equilibrium climate sensitivity. *Earth's Future*, *4*(11), 512–522. https://doi.org/10.1002/2016EF000376

Thorsen, T. J., Kato, S., Loeb, N. G., & Rose, F. G. (2018). Observation-based decomposition of radiative perturbations and radiative kernels. *Journal of Climate*, *31*(24), 10039–10058. https://doi.org/10.1175/JCLI-D-18-0045.1

Vecchi, G. A., Soden, B. J., Wittenberg, A. T., Held, I. M., Leetmaa, A., & Harrison, M. J. (2006). Weakening of tropical Pacific atmospheric circulation due to anthropogenic forcing. *Nature*, *327*(7089), 216–219. https://doi.org/10.1038/nature04744

Wang, C., Yang, W., Vecchi, G., Zhang, B., Soden, B. J., & Chan, D. (2025). Diagnosing the factors that contribute to the intermodel spread of climate feedback in CMIP6. *Journal of Climate*, *38*(3), 663–674. https://doi.org/10.1175/JCLI-D-23-0528.1

Watanabe, M., Kang, S. M., Collins, M., Hwang, Y.-T., McGregor, S., & Stuecker, M. F. (2024). Possible shift in controls of the tropical Pacific surface warming pattern. *Nature*, *630*(8016), 315–324. https://doi.org/10.1038/s41586-024-07452-7

Williams, A. I. L., Jeevanjee, N., & Bloch-Johnson, J. (2023). Circus tents, convective thresholds, and the non-linear climate response to tropical SSTs. *Geophysical Research Letters*, *50*(6), e2022GL101499. https://doi.org/10.1029/2022GL101499

21698996, 2026, 22, Downloaded from https://agupubs.onlinelibrary.wiley.com/doi/10.1029/2026JD047998 by Schweizerische Akademie Der Medizinischen Wissenschaften (Samw), Wiley Online Library on [21/11/2026]. See the Terms and Conditions (https://onlinelibrary.wiley.com/terms-and-conditions) on Wiley Online Library for rules of use; OA articles are governed by the applicable Creative Commons License

Williams, I. N., & Pierrehumbert, R. T. (2017). Observational evidence against strongly stabilizing tropical cloud feedbacks. *Geophysical Research Letters*, *44*(3), 1503–1510. https://doi.org/10.1002/2016GL072202

Wills, R. C. J., Dong, Y., Proistosecu, C., Armour, K. C., & Battisti, D. S. (2022). Systematic climate model biases in the large-scale patterns of recent sea-surface temperature and sea-level pressure change. *Geophysical Research Letters*, *49*(17), e2022GL100011. https://doi.org/10.1029/2022GL100011

Wood, R., & Bretherton, C. S. (2006). On the relationship between stratiform low cloud cover and lower-tropospheric stability. *Journal of Climate*, *19*(24), 6425–6432. https://doi.org/10.1175/JCLI3988.1

Zelinka, M. D., Klein, S. A., & Hartmann, D. L. (2012a). Computing and partitioning cloud feedbacks using cloud property histograms. Part I: Cloud radiative kernels. *Journal of Climate*, *25*(11), 3715–3735. https://doi.org/10.1175/JCLI-D-11-00248.1

Zelinka, M. D., Klein, S. A., & Hartmann, D. L. (2012b). Computing and partitioning cloud feedbacks using cloud property histograms. Part II: Attribution to changes in cloud amount, altitude, and optical depth. *Journal of Climate*, *25*(11), 3736–3754. https://doi.org/10.1175/JCLI-D-11-00249.1

Zelinka, M. D., Klein, S. A., Qin, Y., & Myers, T. A. (2022). Evaluating climate models' cloud feedbacks against expert judgment. *Journal of Geophysical Research: Atmospheres*, *127*(2), e2021JD035198. https://doi.org/10.1029/2021JD035198

Zhou, C., Zelinka, M. D., & Klein, S. A. (2017). Analyzing the dependence of global cloud feedback on the spatial pattern of sea surface temperature change with a Green's function approach. *Journal of Advances in Modeling Earth Systems*, *9*(5), 2174–2189. https://doi.org/10.1002/2017MS001096

21698996, 2026, 22, Downloaded from https://agupubs.onlinelibrary.wiley.com/doi/10.1029/2026JD047998 by Schweizerische Akademie Der Medizinischen Wissenschaften (Samw), Wiley Online Library on [21/11/2026]. See the Terms and Conditions (https://onlinelibrary.wiley.com/terms-and-conditions) on Wiley Online Library for rules of use; OA articles are governed by the applicable Creative Commons License